Sorption of CO_2 and N_2 in Binder-free Zeolite KY studied by a Chromatographic Method

Ezz El Din Wael Ezz El Din Hamdy Aly

Dissertation submitted to:

Escola Superior de Tecnologia de Gestão

Instituto Politécnico de Bragança

To obtain the Master Degree in:

Chemical Engineering

Supervisor:

Professor José António Correia Silva

December 2020

ACKNOWLEDGMENTS

I would like to thank my IPB supervisor Prof. Dr. José António Correia Silva for giving me the opportunity to do this work and for the availability, support and guidance provided throughout the development of my work.

I thank my colleague Lucas Zafanelli for the tremendous help and support, and for sharing your wide knowledge with me. My work wouldn't have been the same without you.

I would like to thank José Luiz Dias Tuesta for measuring the N_2 adsorption-desorption isotherms for the textural data. I also thank my colleague Adriano Henrique for helping me during my early days in the laboratory and for being there whenever I needed anything.

My thanks to all my friends and family who believed in me and gave me all the support, encouragement and inspiration that were essential for me to become who I am today.

Finally, we would like to acknowledge (including the supervisor) Kristin Gleichmann and Chemiewerk Bad Koestritz GmbH for kindly providing the binder-free beads of zeolite KY studied in this work, as well as the Foundation for Science and Technology (FCT, Portugal) and ERDF under Program PT2020 to CIMO (UID/AGR/00690/2019).

ABSTRACT

In the last few decades of industrialization, there has been a significant increase in the concentration of carbon dioxide (CO_2) and other greenhouse gases in the atmosphere, which has a visible harmful effect on the environment we live in today. Regarding that, many organizations around the world have invested heavily in research activities towards CO_2 capture and storage. Adsorption processes are characterized with low energy costs and can involve low investment in terms of both initial cost and space required.

In this work, the adsorption equilibrium of CO_2 and N_2 in commercial binder-free beads of KY zeolite has been studied between 313 K and 423 K and pressure up to 3.5 bar using a gas chromatographic technique (frontal chromatography/breakthrough technique). At the temperature of 313 K, the results showed that the amount adsorbed of CO_2 in binder-free KY is up to 6.42 $mol.kg^{-1}$ with heats of adsorption of 41.4 $kJ.mol^{-1}$. The amount adsorbed of N_2 at similar conditions is much less compared to CO_2 where it doesn't exceed 0.68 $mol.kg^{-1}$ being the heat of adsorption around 21.1 $kJ.mol^{-1}$. The adsorption equilibrium data were fitted with the Langmuir and the dual-site Langmuir (DSL) models and compared with other Y zeolites modified by cation exchange available in literature. The comparisons showed that the commercial binder-free KY studied in this work is a good alternative adsorbent for the adsorption CO_2, being also characterized by a high adsorption capacity at low pressure (below 1 bar) when compared to other cation exchanged materials. In addition, the binder-free type KY was responsible for an improvement for up to 20 % in CO_2 loading compared to the standard binder beads of KY zeolite.

Binary-component experiments CO_2/N_2 were also carried out under typical post-combustion conditions (15% CO_2 / 85% N_2) at 313, 373 and 423 K. At 313 K, the selectivity of CO_2 over N_2 goes over 105 at low pressures below 0.1 bar. At 298 K, the competitive working capacity between 0.03 and 1 bar is equal to 4.52 $mol.kg^{-1}$, which is a relatively high value when compared with materials such as: Mg-MOF-74 and zeolite 13X. Generally, the results show that binder-free KY works best in the low-pressure region and therefore, is a promising adsorbent for the recovery of CO_2 from post-combustion streams.

Also, the binary breakthrough curves CO_2/N_2 onto the binder-free zeolite KY were simulated using a numerical technique developed in MATLAB. The results showed that the zone spreading of the breakthrough curves in the bed are completely dominated by axial dispersion. The effect of the flowrate of N_2 to clean the bed was also studied by simulation and the results showed that it is possible to reduce the total volume of N_2 used in the desorption step by at least 13% while reducing the N_2 purge time up to 71%.

LIST OF CONTENT

LIST OF FIGURES 7

LIST OF TABLES 7

NOMENCLATURE 9

1. INTRODUCTION 13

1.1. Threat of Carbon Dioxide (CO_2) 13

1.2. Post-combustion capture of CO_2 from flue gas 14

1.3. Molecular sieves – Zeolites 15

1.3.1. Type A 16

1.3.2. Type X, Y (Faujasite) 17

1.3.3. Mordenite 19

1.3.4. Binder-free beads 20

1.3.5. Metal-Organic-Framework 21

1.4. Adsorption processes 21

1.4.1. CO_2 Adsorption behavior in different adsorbent materials 22

1.4.2. Experimental techniques for gas adsorption studies 23

2. THEORY 27

2.1. Effect of zeolite structural characteristics on CO_2 adsorption 27

2.1.1. Basicity effect on CO_2 Adsorption 27

2.1.2. Si/Al ratio effect on CO_2 Adsorption 27

2.1.3. Polarization, distribution, number and size of exchangeable cations effect on CO_2 Adsorption 28

2.1.4. Importance of cation exchange in the performance of the zeolite on CO_2 Adsorption 29

2.2. Adsorption Equilibrium Loading Measurement by Chromatographic Breakthrough Experiments 30

2.3. Adsorption Equilibrium Isotherm Models 30
2.3.1. Langmuir Model 30
2.3.2. Dual-site Langmuir Model 31
2.4. Adsorbent Screening Metrics 33
3. EXPERIMENTAL STUDIES 35
3.1. Breakthrough Experimental Apparatus 35
3.2. Experimental Procedures 37
3.3. Commercial binder-free Zeolite KY 38
4. RESULTS AND DISCUSSION 39
4.1. Adsorption Equilibrium of CO_2 on binder-free KY 39
4.2. Comparison of CO_2 adsorption equilibrium data in different ion-exchanged zeolites 45
4.3. Adsorption equilibrium of N_2 on binder-free KY 48
4.4. Binary-component adsorption of CO_2 / N_2 on binder-free KY 54
4.5. Adsorbent Metrics on CO_2/ N_2 Isotherms 59
4.6. Simulation of Binary Adsorption of CO_2/N_2 on binder-free zeolite KY 61
5. CONCLUSION 69
REFERENCE 71
APPENDIX 78
A- Fixed bed Breakthrough Experiment 78
B- Determination of Textural Data for binder-free KY Zeolite 80
C- Comparisons of CO_2 adsorption equilibrium data in different ion-exchanged zeolites 81
D- Simulation Correlations 84

LIST OF FIGURES

Figure 1: Schematic representation of A and XY type zeolites. [19] 17
Figure 2: Framework structure of Faujasite-type zeolites. [20]..... 18
Figure 3: Schematic presentation of the Mordenite structure. [16] 19
Figure 4: N_2 adsorption isotherms (at 77 K) of zeolite NaMSX powder, binder containing and binder-free molecular sieves. [26] 20
Figure 5: Schematic drawing of the experimental set-up used to perform single- and multi-component breakthrough experiments to measure the adsorption equilibrium. 35
Figure 6: Adsorption equilibrium isotherms of CO_2 on zeolite KY. 39
Figure 7: Adsorption equilibrium isotherm of CO_2 on binder-free KY zeolite and fitting with the Langmuir model. 41
Figure 8: Plot of ln p over 1/T at fixed coverages for calculating the isosteric heat of CO_2. 42
Figure 9: Adsorption equilibrium isotherms of CO_2 on binder-free KY zeolite and fitting using the DSL model. 43
Figure 10: Isosteric heat of adsorption as a function of CO_2 coverage experimental and numerically predicted by the DSL model in binder-free zeolite KY. 44
Figure 11: Comparison of CO_2 adsorption isotherms in different ion-exchanged zeolites at 323 K [41]. *The data for binder-free KY was measured in this work. 45
Figure 12: Comparison of adsorption isotherms in low pressure region at 333 K on cation exchanged zeolites Y. [41]..... 46
Figure 13: Isosteric Heat Comparison of CO_2 on alkali-metal exchanged FAU zeolites [41]. * The data for binder-free KY was measured in this work. 46
Figure 14: Adsorption Equilibrium Isotherms of N_2 on zeolites KY. 48
Figure 15: Adsorption equilibrium isotherms of N_2 on binder-free KY zeolite and fitting using the Langmuir model. 50
Figure 16: Plot of ln p over 1/T at fixed coverages for N_2 on binder-free KY. 51
Figure 17: Comparison of N_2 adsorption isotherms in binder-free KY and NaY at different temperatures [58]. *The data for binder-free KY was measured in this work. 52
Figure 18: Adsorption Equilibrium Isotherms of CO_2 and N_2 on zeolites KY..... 53

Figure 19: Adsorption (a) and desorption (b) breakthrough curves of binary mixtures CO_2 (15%) /N_2 (85%) on binder-free zeolite KY at 313 K. 55
Figure 20: Adsorption (a) and desorption (b) breakthrough curves of binary mixtures CO_2 (15%) /N_2 (85%) on binder-free zeolite KY at 373 K. 56
Figure 21: Adsorption (a) and desorption (b) breakthrough curves of binary mixtures CO_2 (15%) /N_2 (85%) on binder-free zeolite KY at 423 K. 57
Figure 22: Adsorption equilibrium isotherms of binary-component system CO_2 / N2 on binder-free KY zeolite and fitting using the extended DSL model. 58
Figure 23: Selectivity of CO_2 / N_2 on binder-free KY at different temperatures. 60
Figure 24: Influence of overall mass transfer coefficient on numerical breakthrough curve of CO_2 at 313 K and 0.15 bar partial pressure balanced with N_2 64
Figure 25: Influence of Peclet number on numerical breakthrough curve of CO_2 at 313 K and 0.15 bar partial pressure balanced with N_2. 64
Figure 26: Adsorption and desorption breakthrough curves for CO_2 on binder-free zeolite KY at 313 K. The column is first saturated with N_2 (1 bar), and then, it is fed a gas mixture (15% CO_2 balanced with N_2). Experimental = symbols; Lines = simulations. 66
Figure 27: Adsorption and desorption breakthrough curves for CO_2 on binder-free zeolite KY at 373 K. The column is first saturated with N_2 (1 bar), and then, it is fed a gas mixture (15% CO_2 balanced with N_2). Experimental = symbols; Lines = simulations. 66
Figure 28: Adsorption and desorption breakthrough curves for CO_2 on binder-free zeolite KY at 423 K. The column is first saturated with N_2 (1 bar), and then, it is fed a gas mixture (15% CO_2 balanced with N_2). Experimental = symbols; Lines = simulations. 67
Figure 29: Profiles of CO_2 normalized concentrations during desorption with various N_2 purge rates at a fixed temperature of 373 K. 68
Figure 30: TCD Signal Output 78
Figure 31: Corrected Signal 78
Figure 32: Breakthrough Curve 79
Figure 33: N_2 adsorption-desorption isotherms at 77K of the material. 80
Figure 34: Comparison of CO_2 adsorption isotherms in binder-free KY and NaY at high pressure at 303 K [60]. 81

Figure 35: Comparison of CO_2 adsorption isotherms in binder-free KY and NaY at different temperatures [58]. 82
Figure 36: Adsorption heats comparison of CO_2 on alkali-metal exchanged zeolites. [57]..... 82
Figure 37: Comparison of CO_2 adsorption isotherms in different binder-free zeolites at 323 K [20]. *The data for binder-free KY was measured in this work. 83

LIST OF TABLES

Table 1: Different zeolites with corresponding Si/Al ratio. [15] 16
Table 2: Column, Adsorbent and Operating Conditions. 37
Table 3: Textural properties of the binder-free KY zeolite studied in this work. 38
Table 4: Experimental conditions of all runs at 313, 373 and 423 K to study the CO_2 adsorption on binder-free KY zeolite. 40
Table 5: Adsorption equilibrium Langmuir model parameters for CO_2 on binder-free KY zeolite. 41
Table 6: Adsorption equilibrium DSL model parameters for CO_2 on binder-free KY zeolite. 43
Table 7: Experimental conditions of all runs at 313, 373 and 423 K to study the N_2 adsorption on binder-free KY zeolite. 49
Table 8: Adsorption equilibrium Langmuir model parameters for N_2 on binder-free KY zeolite.50
Table 9: Binary-component experimental conditions of runs at 313 K, 373 K and 423 K. 54
Table 10: Adsorption equilibrium DSL model parameters for binary-component system of CO_2/ N_2 on binder-free KY zeolite. 58
Table 11: Comparison of Adsorbent Metrics with different zeolites in CO_2 (15%) /N_2 (85%) stream. 59
Table 12: Mathematical Model Equations for Fixed Bed Adsorption simulator. 61
Table 13: Estimated parameters of axial dispersion and mass-transfer resistances from the method of moments for experimental breakthrough curves of CO_2/N_2 mixture. 63
Table 14: Calculated model parameters for the simulation of binary adsorption (Ads) and desorption (Des) breakthrough experiments. 65
Table 15: Correlations for estimating model parameters used in simulations 84

NOMENCLATURE

a_p	Specific area of the pellet (m^{-1})
a_c	Specific area of the column (m^{-1})
b_i	Adsorption affinity constant of component i (bar^{-1})
b_∞	Pre-exponential factor of the affinity constant (bar^{-1})
C	Total gas concentration (mol m^{-3})
C_{io}	Feed gas-phase concentration at the inlet of the fixed bed (mol m^{-3})
C_{pg}	Heat capacity of gas (J mol^{-1} K^{-1})
C_{ps}	Heat capacity of solid (J mol^{-1} K^{-1})
d_p	Pellet diameter (m)
d_c	Column diameter (m)
D_{AB}	Diffusivity of A in B (m^2 s^{-1})
D_{ax}	Axial mass dispersion coefficient (m^2 s^{-1})
D_c	Crystal diffusivity (m^2 s^{-1})
D_k	Knudsen diffusivity (m^2 s^{-1})
D_m	Molecular diffusion (m^2 s^{-1})
D_p	Effective diffusivity (m^2 s^{-1})
$F_{f,i}$	Feed molar flow rate of component i at the inlet of the bed (mol m^{-2} s^{-1})
F_i	Feed molar flow rate of component i at the outlet of the bed (mol m^{-2} s^{-1})
h_p	Film heat transfer coefficient (W m^{-2} K^{-1})
h_w	Wall heat transfer coefficient (W m^{-2} K^{-1})
k'	Overall effective rate coefficient (W m^{-2} K^{-1})
K	Dimensionless Henry´s law equilibrium constant (-)
K_{LDF}	Linear Driving Force coefficient (s^{-1})
K_{ax}	Effective axial bed thermal conductivity (W m^{-1} K^{-1})
L	Length of column (m)
Nu	Nusselt number

p_i	Partial pressure of component i (bar)
P	Total pressure of column (bar)
Pe	Peclet number
q_i	Adsorbed phase concentration of component i (mol kg^{-1})
$\bar{q}_i$	Average adsorbed phase concentration of component i (mol kg^{-1})
q_{cal}	Calculated adsorption capacity (mol kg^{-1})
$\overline{q_{cal}}$	Average calculated adsorption capacity (mol kg^{-1})
q_m	Maximum adsorbed phase concentration (mol kg^{-1})
r_p	Pore radius (Å)
R_c	Crystal radius (m)
R_p	Pellet radius (m)
R	Universal gas constant (J mol^{-1} K^{-1})
Re	Reynolds number
S_{BET}	BET surface area (m^2 g^{-1})
S_{ext}	External surface area (m^2 g^{-1})
$S_{Langmuir}$	Langmuir surface area (m^2 g^{-1})
S_{mic}	Micropore surface area (m^2 g^{-1})
t	Time (s)
t_n	Saturation time (s)
T	Temperature in bulk gas phase (K)
T_s	Temperature in solid phase (K)
T_w	Wall temperature (K)
v	Superficial velocity (m s^{-1})
v_i	Interstitial velocity (m s^{-1})
V_c	Column volume (m^3)
V_{mic}	Micropore volume (mm^3 g^{-1})
V_{Total}	Total pore volume (mm^3 g^{-1})
V_{mic}	Average pore width (nm)
y_i	Molar fraction of sorbate species i in the bulk phase
z	Axial coordinate in bed (m)

Greek letters

α_P	Pure component selectivity (-)
α_C	Competitive component selectivity (-)
β_P	Pure working capacity (mol kg^{-1})
β_C	Competitive working capacity (mol kg^{-1})
ΔH_i	Isosteric heat adsorption of species i (J mol^{-1})
ε_b	Bed porosity
ε_p	Solid porosity
ρ_s	Apparent adsorbent density (kg m^{-3})
τ	Tortuosity

Abbreviations

GHG	Greenhouse Gas
CCS	Carbon Capture Storage
MOFs	Metal-Organic Frameworks
NGCC	Natural Gas Combined Cycle
IGCC	Integrated Gasification Combined Cycle
FAU	Faujasite-type
CEC	Cation Exchange Capacity
PSA	Pressure-Swing Adsorption
VSA	Vacuum-Swing Adsorption
TSA	Thermal-Swing Adsorption

1. INTRODUCTION

1.1. Threat of Carbon Dioxide (CO_2)

The global environment is a major issue today, and global warming in particular is the focus of much attention. Accumulation of greenhouse gases in the atmosphere is responsible for increased global warming of our planet. [1]

The removal and recovery of CO_2 from hot gas streams is becoming increasingly significant in the field of energy production. The combustion of fossil fuels such as coal or natural gas releases large volumes of CO_2 into the environment and has thereby become one of the most serious global problems. [2]

Although carbon dioxide is removed from the atmosphere through plants in the biological CO_2 cycle, large amount of current and future anticipated CO_2 is beyond the capacity of our greens. In addition, this natural cycle falls short when eventually plants and animals decay and begin to release captured CO_2 into the atmosphere, making an ineffective natural cycle. [3, 4].

It is assumed that the increasing concentration of carbon dioxide, mainly from flue gas, automobile, and landfill emissions in the atmosphere is the major contributor to this problem with more than 80% of total GHG emissions. [1] For this reason, the chosen greenhouse to focus on in this study is carbon dioxide.

Numerous choices are there to reduce CO_2 emissions in the atmosphere such as improving power plant efficiency, replacement of coal by natural gas, introducing higher thermal efficiency combined cycles of steam and gas for power generation, shifting to renewable resources and CCS. [5]

Generally, these techniques are not applicable to the large number of existing fossil fuel-fired power plants and other power-consuming units. In 2019, around 84% of global primary energy came from coal, oil and gas. [6] This source of energy cannot be weeded out rapidly. Fossil fuels will be relied on as the primary source of energy for the next several decades. Therefore, an extensive research effort would be needed to improve the CO_2 capture and storage technologies. [7]

There are three basic CO_2 capture routes: (1) pre-combustion capture (via oxygen-blown gasification); (2) oxy-fuel combustion, i.e. removing nitrogen before combustion; and (3) post-combustion capture. In these processes, up to 90 % of CO_2 capture is possible to be achieved. This percentage can be increased, but elevated cost is the main constraint. [8]

1.2. Post-combustion capture of CO_2 from flue gas

The generation of carbon dioxide is inherent in combustion of fossil fuels, and the efficient capture of CO_2 from industrial operations is regarded as an important strategy through which to achieve a significant reduction in atmospheric CO_2 levels. Capture of CO_2 from flue gases produced by combustion of a carbon-based fuels, such as coal or natural gas, is referred to as post-combustion capture. Instead of being discharged directly to the atmosphere, flue gas is passed through equipment which separates most of the CO_2. The CO_2 is fed to a storage reservoir and the remaining flue gas is discharged to the atmosphere. [9]

One of the biggest challenges in post-combustion capture is separating the relatively low concentration of CO_2 from the large amounts of nitrogen in the flue gas. Flue gases from natural gas combined cycle (NGCC) plants typically contains around 5% CO_2 by volume compared to a CO_2 concentration of 12-15% in flue gases from fuel-fired plants. [10]

Adopting the post-combustion capture route avoids the potentially long time periods required to develop cost-effective coal-derived syngas separation technologies, hydrogen turbine technology, and fuel-cell technology, etc. It can also provide means of CO_2 capture in the near-term for new and existing stationary fossil fuel-fired power plants. [8]

Current adsorption technologies which propose the capture of CO_2 are costly and energy intensive. Membrane technology is an attractive CO_2 capture options because of the advantages such as energy-efficient passive operation, no use of hazardous chemicals, and tolerance to acid gases and oxygen. However, an important challenge associated with membrane technology is how to create the driving force efficiently, because the feed flue gas is at ambient pressure and contains a relatively low CO_2 content. [8]

Solid sorbents are another promising capture technology. These sorbents can either react with the CO_2 or it can be adsorbed onto the surface. Chemical sorbents that react with the CO_2 in the flue gas can be comprise of a support, usually of high surface area, with an immobilized amine or other reactant on the surface. Physical adsorbents can separate the CO_2 from the other flue gas

constituents, but do not react with it. Instead, they use their cage-like structure to act as molecular sieves. These sorbents can be regenerated using a pressure swing or temperature swing adsorption. Physical adsorbents such as zeolites is safe for the local environment, and are generally inexpensive to manufacture. [8]

1.3. Molecular sieves – Zeolites

The word zeolite is derived from the Greek "zeo" meaning boil and "lithos" meaning stone. Zeolites are crystalline metal aluminosilicates with a three-dimensional interconnecting network structure of silica and alumina tetrahedra. Some occur naturally and some have only been produced synthetically. Zeolites are of interest because they have the capacity to sorb gases, vapours and liquids, to catalyse reactions, and to act as cation exchangers. [11]

Zeolites have a honeycomb or cage-like structure, which has been identified as the world's only mineral with naturally occurring negative charge. Conventional zeolites have interlocking tetrahedron of silicate and aluminate in various regular arrangements through shared oxygen atoms. Substitution of Si with Al (or other metals) leads to a negative charge on the framework. The charge is balanced by exchangeable cations usually alkaline or alkaline-earth metals (e.g., Na^+, K^+, Ca^{2+}, Mg^{2+}). Water molecules and cations are free to move within the crystals and so can be readily removed or exchanged respectively. These cations are located in the channels and cavities throughout the pores structure. [7, 12, 13]

Furthermore, diffusion through these pores may be also heavily influenced by their interaction with the surface. For every alumina tetrahedron in the zeolite structure, a positive charge is required to make the entire structure neutral. Thus, the lower silica alumina ratio, the greater the number of cationic charges. The electric field and basicity of this material normally vary inversely with the Si/Al ratio. Lower ratio of Si/Al has higher basicity. Basicity increases the specific interaction between CO_2 and zeolites that resulted in high value of CO_2 adsorption. [14] Different zeolite families with their corresponding Si/Al ratio is presented in Table 1.

There are different types of natural and synthetic zeolites such as Type A (4A and 5A Zeolites), Faujasite (Type X, Y), Mordenite, and Clinoptilolite. Each of them exhibits different sizes, Si/Al ratio, ionic forms, chemical structure, adsorptive properties, CEC, and many other specifications. This variety of zeolites brings a tremendous versatility of adsorbents available for the industry today.

Carbon may also be formed into a molecular sieve, but it is not a zeolite as it contains no silica or alumina. It consists of elementary graphite microcrystallites which are stacked together in random orientation, and the spaces between these crystals form the micropores. This difference in composition leads to distinct differences in adsorption properties. [16]

Table 1: Different zeolites with corresponding Si/Al ratio. [15]

Zeolite Type	Si/Al Ratio Ranges
Analcite	1.00 – 3.00
Clinoptilolite	2.92 – 5.04
Chabazite	1.43 – 4.18
Edingtonite	1.00 – 2.00
Erionite	3.05 – 3.99
Faujasite	1.00 – 3.00
Ferrierite	3.79 – 6.14
Heulandite	2.85 – 4.31
Laumontite	1.95 – 2.25
Mordenite	4.19 – 5.79
Phillopsite	1.45 – 2.87
Stibilite	2.50 – 5.00

1.3.1. Type A

Type A is one of the most commonly used zeolite, which does not occur naturally. It's been used in multiple practical applications including separation, drying and purification of gases. There are 3 common ionic forms of A zeolite: potassium (3A), sodium (4A) and calcium (5A) forms. [16]

The structure of Zeolite A is shown schematically in Figure 1. The pseudo cell consists of 8 sodalite cages located at the corners of a cube and joined through four-membered oxygen rings. This arrangement forms a large polyhedral cage of free diameter about 11.4 Å accessible through eight-membered oxygen windows. Stacking these unites in a cubic lattice gives a three-dimensional isotropic channel structure, constricted by eight-membered oxygen rings.

As Ruthven and Breck [17, 18] described, each pseudo cell contains 24 tetrahedral (AlO_2 or SiO_2) units and as the Si/Al ratio in zeolite A is always close to 1, there are 12 univalent exchangeable cations per cell. Three distinct cation sites have been identified; near the centers of the six-rings in the eight corners of the central cavity (type I), in the eight-rings (type II), and on

the cage wall in close proximity to a four-ring (type III). With most cations the type I sites are preferentially occupied, followed by the type II sites, and the type III sites are filled only after all sites of types I and II have been occupied. In the sodium form (4A) there are 12 cations per cage. These are accommodated in the eight type I sites and three type II sites (the six eight-rings are each shared between two cages) with one cation in a type II site. All windows are therefore partially obstructed by a sodium cation and the effective aperture of the sieve is therefore reduced from about 4.4 to 3.8 Å. If the Na^+ cations are exchanged for Ca^{2+} or Mg^{2+} the number of cations per cell decreases. At 67% exchange there are only eight cations per cell and all these can be accommodated in this type I sites. Therefore, in Ca^{2+} or Mg^{2+} (5A) the effective aperture is increased and somewhat larger molecules can penetrate.

Since the diameter of the potassium ion is greater than that of sodium, a sieve with a smaller effective aperture (3A sieve) is obtained by potassium exchange. The 3A sieve is widely used for drying reactive hydrocarbons such as olefins since the small pre size prevents penetration of the lattice and thus the possibility of reaction. [17]

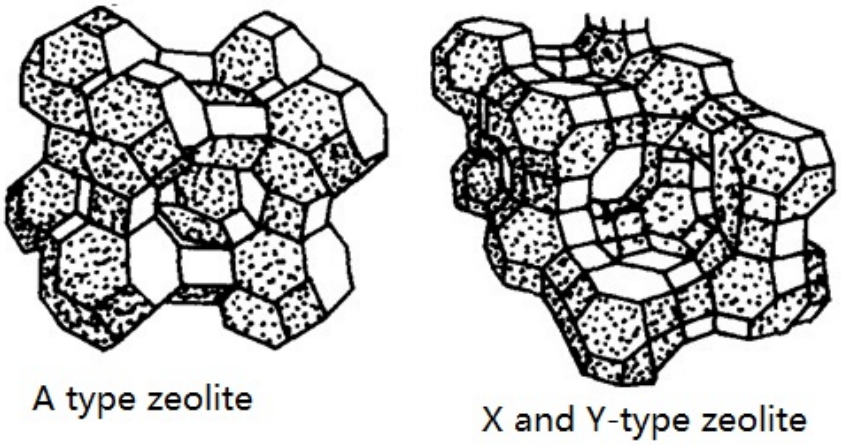

Figure 1: Schematic representation of A and XY type zeolites. [19]

1.3.2. Type X, Y (Faujasite)

Zeolite Y, together with zeolite X, belongs to the family of aluminosilicate molecular sieves with a faujasite-type structure (FAU). Type X zeolite is identical to type Y zeolite with the exception that type Y has a higher Si/Al atomic ratio (1.0 – 1.5 for X as compared to 1.5 – 3.0 for Y). There is a corresponding difference in number of exchangeable univalent cations, which varies from about 10-12 per cage for X to as low as 6 for high silica Y. [17, 18] These cations are known to populate three main sites within the cages as shown in Figure 2: sites I/I' in the sodalite cages,

sites II/II" at the hexagonal rings inside the cavities, and sites III/III' at the entrance of the supercage. X zeolites can contain cations at all sites. Y zeolites typically have no cations located at sites III and III'. The cations located at sites I and I' are within the sodalite cages and are generally not accessible for interaction with most adsorbate molecules, as Walton *et al.* [20] have described in their advanced study of CO_2 adsorption in Y and X zeolites.

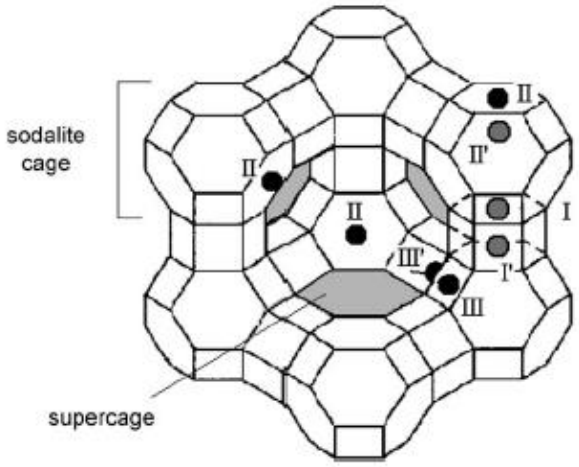

Figure 2: Framework structure of Faujasite-type zeolites. [20]

The 24-tetrahedracuboctahedral units (sodalite cages) in the FAU framework type are arranged in a way that they are connected via hexagonal prisms (double 6-rings) forming a 3-dimensional porous channel structure along, characterized by 12-oxygen ring window openings with the aperture of around 8 Å and supercages of approximately 12 Å [21]. There are many ionic forms of type X zeolite, one of the more common being the calcium exchanged version (10 X zeolite), which contains approximately 41 Ca^{++} and 6 Na^{+} ion per cage. Strontium, barium, and potassium have also been used in various ionic combinations. The location of ions in the large faujasite cage depend upon the nature and number of ions, and on the presence of trace quantities of moisture. The faujasitic structure demonstrates extreme versatility in gas separations and catalytic applications through ion exchange and metal impregnation. The 8.4 Å pore openings in type X zeolite is the largest in the common commercially produces zeolites, and therefore generally allow quick diffusion into the pore structure. The large 192 tetrahedral unit cells have a void volume of approximately 7500 $Å^3$. The pore volume and diameter are therefore affected relatively less by ion exchange than those of type A zeolite. Therefore, with small gases the many ionic forms may be used freely without worry of significant pore blockage due to the various ion sizes and locations [16, 17].

1.3.3. Mordenite

Mordenite is a zeolite mineral usually coming in Na^+ and H^+ cationic forms. It occurs naturally in altered volcanic deposits and in marine sediments. It may also be synthesized. Mordenite's molecular structure is a framework containing chains of five-membered rings of linked silicate and aluminate tetrahedra (four oxygen atoms arranged at the points of a triangular pyramid about a central silicon or aluminum atom). [22]

The Si/Al ratio in both natural and synthetic forms is generally close to 5 but the aluminum content of the framework may be decreased substantially by acid leaching without significant loss of crystallinity. Unlike the other zeolites, the channel structure of mordenite is one-dimensional for large molecules, and two-dimensional for the diffusion of very small molecules, as shown in Figure 3. The main channel, which is formed from twelve-membered oxygen rings, has a nominal free diameter of 6.7-7.0 Å. However, natural mordenite behaves as a small-port zeolite and even small molecules such as methane and ethane are only slowly adsorbed. This appears to be due to one-dimensional structure that makes mordenite very susceptible to pore blockage due to the presence of extraneous material. The sieve may be opened by controlled acid leaching which evidently removes some of the detrital material from the channels. [16]

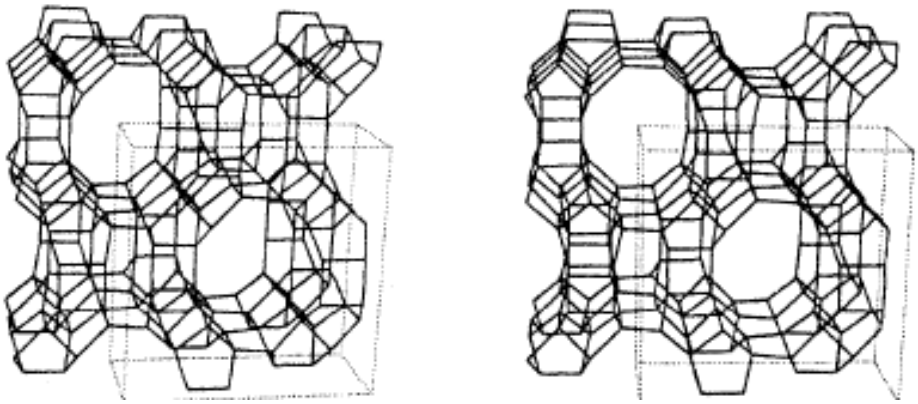

Figure 3: Schematic presentation of the Mordenite structure. [16]

A synthetic type of modernite known as "large port" mordenite has been prepared and it is apparently free of this extraneous material, displaying the adsorption characteristics expected for a 7 Å pore size. The unit cell void volume of mordenite has been determined to be approximately 800 $Å^3$. [16, 22]

1.3.4. Binder-free beads

Normally, most zeolites are formed by transforming the adsorbents zeolite powder into molecular sieves. This transformation reduces up to 20% of the capacity of the pellet, which is the amount of adsorptive inert clay binder generally used to give the necessary mechanical strength to the beads in order to be used in packed-columns and at the same time to reduce pressure drop. To increase the working capacity the binder can also be converted to zeolite matter leading to the so-called binder-free pellets or bead. [18, 23].

Recently, this technology has been recovered and applied for the synthesis of binder-free beads such as 13X zeolite and 5A zeolite, where the non-zeolitic components (temporary binder) is converted to zeolite during a hydrothermal conversion after the manufacturing procedure. In this way, the resulting binder-free pellet can increase the working capacities of existing zeolite adsorbent technologies. [23, 24, 25].

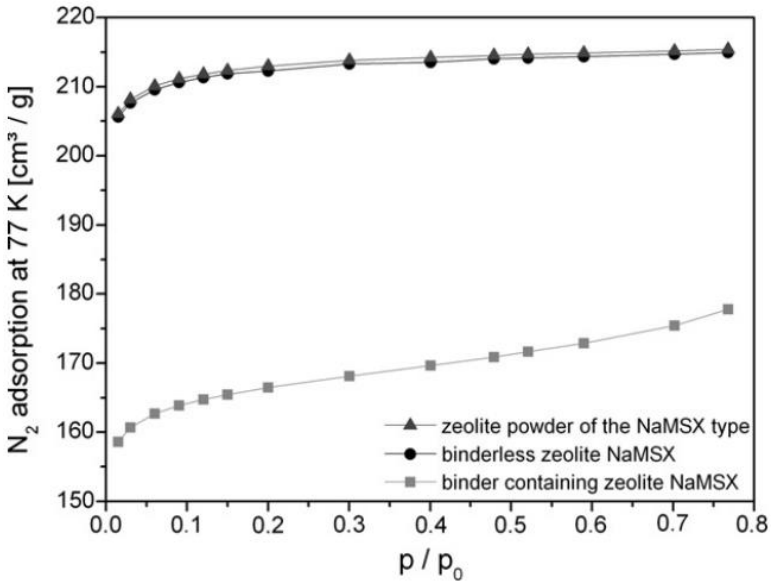

Figure 4: N_2 adsorption isotherms (at 77 K) of zeolite NaMSX powder, binder containing and binder-free molecular sieves. [26]

Figure 4 shows a comparison of the static adsorption capacity of zeolite NaMsX powder of binder and binder-free molecular sieves. As expected, such binder-free molecular sieves show an enhanced static adsorption capacity as compared to binder containing molecular sieves of the same zeolite type. Due to the existence of a unique secondary pore system in advantageous combination with the 100% zeolite content the new material shows remarkably better dynamic adsorption properties in comparison to the conventional material. [26]

1.3.5. Metal-Organic-Framework

A new class of adsorbents named Metal-Organic Framework (MOFs) are focused being clear that in future they can be an excellent alternative to zeolite adsorbents due to its high surface area and pore volume. However, MOFs need to be further refined regarding its production in large scale, chemical and thermal stability, which are properties already well-established in zeolites. [23]

1.4. Adsorption processes

Adsorption processes involves separation of a substance from one phase (gas or liquid) accompanied by its accumulation or concentration at the surface of another (solid). The substance being adsorbed is the adsorbate (or solute) and the solid on which adsorption occurs is the adsorbent. An unbalanced force of attraction on the surface of the solid is generally responsible for the adsorption to occur. Adsorption is thus different from absorption, a process in which material transferred from one phase to another (e.g. liquid) interpenetrates the second phase to form a "solution". The term sorption is a general expression encompassing both processes. [27]

The adsorption of gases and solutes is usually described through the so-called isotherms, that is, the amount of adsorbate on the adsorbent as a function of its pressure (if gas) or concentration (for liquid phase solutes) at constant temperature.

In the process of gas adsorption, the molecules of the gas temporarily depart from the gas phase when it comes to the vicinity of the solid surface and undergoes an interaction with it. Molecules in this new condensed state remain for a short period and then return to the gas phase. The duration of this stay depends on the characteristic of the adsorbing surface and the adsorbate, the number of gas molecules that encounter the surface, their kinetic energy, and other factors such as capillary forces, surface heterogeneities. Besides the characteristics of adsorbates and adsorbents, the adsorption temperature and pressure also play an important role in gas encapsulation in solid matrices. The effect of temperature on the adsorption capacity depends greatly on the nature of solid matrices and type of adsorbing gas. For example, in hydrogen adsorption on carbon nanotubes, lower temperature favors adsorption. [7, 28, 29]

1.4.1. CO_2 Adsorption behavior in different adsorbent materials

1.4.1.1. Carbon-based adsorbents

It is well known that carbon-based adsorbents exhibit a high adsorption capacity towards CO_2 at ambient temperature and pressure. [30]

Owing to their low cost, high surface area, high amenability to pore structure modification and surface functionalization, and relative ease of regeneration, carbon-based materials are considered to be one of the most promising adsorbents for capturing CO_2 in integrated gasification combined cycle (IGCC) processes for energy generation and hydrogen production. However, the CO_2 adsorption on carbon materials is ‘‘physical’’ and weak, which makes these adsorbents sensitive to temperature and relatively poor in selectivity. [31]

1.4.1.2. Zeolites

Zeolites are very important adsorbents for CO_2 gas separation and purification because CO_2 has a high linear quadrupole moment which interacts with intra-zeolite cations. [32]
As we discussed before, the electric field and basicity of the zeolite material normally vary inversely with the Si/Al ratio. Lower ratio of Si/Al has higher basicity. Basicity increases the specific interaction between CO_2 and zeolites that resulted in high value of CO_2 adsorption. The channel diameter of zeolites ranges from 300 to 1000 pm, while kinetic diameter of CO_2 is about 209 pm. As a result, zeolites can also separate CO_2 by molecular sieving effect. [12]

The polarity and the presence of pores make the zeolite an efficient shape-selective sorbent for a broad range of separation applications. Relatively large energetic dipole and quadrupole moment in the molecules is also one appealing factor for selective adsorption of gases in zeolites. [32] Gases having large quadrupole moment and polarizability interact more easily with the electric field created by the structural cations of zeolites (Na+, K+, Ca2+, Mg2+), which favors adsorption of CO_2 on zeolites. The order of adsorption capacity of gases on zeolites is carbon dioxide followed by nitrogen, methane, and hydrogen. This is explained by the fact that CO_2 has greater quadrupole moment and polarizability than the other gases. [34]

Zeolites are generally considered to have strong adsorption behavior for moisture. Sometimes, the moisture contents of zeolites reach 20 % of its own weight. The presence of

moisture content significantly decreases adsorption capacity of cationic zeolites by favoring the formation of bicarbonates and decreasing strength and heterogeneity of the electric field. Additionally, CO_2 adsorption capacity increases with the gas phase pressure and decreases with the rise in adsorption temperature. [7]

A study of zeolites made in IAU on the feasibility of CO_2 adsorption by solid adsorbents revealed that there are 50 types of natural and 150 types of synthetic zeolites. The presence of impurity in naturally occurring zeolites makes them less favorable for adsorption of CO_2. Chabazite in naturally occurring zeolites and 13X and 5A in synthetic zeolites are better adsorbents for CO_2 separations. [7]

1.4.1.3. MOFs

Metal–organic frameworks (MOFs) are one class of crystalline adsorbent materials that are believed to be of huge potential in CO_2 capture applications because of their advantages such as ultrahigh porosity, boundless chemical tunability, and surface functionality over traditional porous zeolites and activated carbon. [35] However, the CO_2 adsorption and separation properties of MOFs are often discussed only from a scientific point of view, without going into the details of application-related aspects. The demands in terms of adsorption capacity, selectivity, pressure range, stability, and so on differ from one application to another. Hence, there is no such thing as a good general CO_2 adsorbent, as it is a must to identify the application for which the adsorbent is best suited. [36]

1.4.2. Experimental techniques for gas adsorption studies

In gas adsorption studies, the adsorption capacity and the diffusivity are the two key parameters commonly measured. The capacity represents the amount of gas adsorbed per unit adsorbent and the diffusivity of gases in molecular sieves represents how fast the gas diffuse into the adsorbent.

Determination of these parameters involves measurements of the adsorbent-adsorbate system response to a change in conditions. The measured capacities and diffusivities can be used to predict selectivities, and to choose and design adsorption processes. The most common ways to do these measurements are using the volumetric, gravimetric, and gas chromatographic methods.

1.4.2.1. Volumetric method

The volumetric method consists of expanding a gas from a pressure cell into an evacuated adsorption cell containing a clean adsorbent during an isothermal process. The volumes of both cells are known. Each measurement of the total quantity of gas admitted into the system and of the amount of gas remaining in the gas phase at the adsorption equilibrium is determined by P–V–T measurements before and after adsorption by using a real gas equation of state. The amount adsorbed is calculated by a mass balance on the gas phase before and after adsorption. [37] In other words, as the gas is adsorbed and allowed to come to equilibrium the measured decrease in the closed system pressure yields the adsorbed under the given conditions. This method has been used extensively to determine adsorption isotherms and measure diffusivities as it has the advantage of being able to be combined with other methods. However, it takes a long time for the process to reach equilibrium and it requires equipment with very sensitive pressure measurements.

1.4.2.2. Gravimetric method

The gravimetric method consists of exposing a clean adsorbent sample to a pure gas at constant temperature. The change in the weight of the adsorbent sample as well as pressure and temperature are measured when equilibrium is reached. This method allows the direct measurement of the amount adsorbed which was not the case for the volumetric method. It is considered as a well-established and accurate technique. Main advantage is that the amount of gas adsorbed or desorbed is measured directly and by measuring the weight change with time, diffusivities can also be calculated. However, the main disadvantage is, in addition to the required high sensitivity of the scale (balance), the difficulty of mounting and maintaining such a balance to be independent of any interference that may arise. [37, 38]

The two equilibrium methods are therefore favored for systems with relatively slow diffusion and moderate conditions (temperature and pressure).

1.4.2.3. Gas chromatography method

The gas chromatographic methods provide an alternative to conventional gravimetric or volumetric methods of determining adsorption equilibrium isotherms. Gas chromatograph works by using a non-adsorbing carrier into which an adsorbable component is injected by a syringe or added (to create a gas mixture) using a sample valve. Since the velocity of the concentration wave

through a chromatographic column is determined by the slope of the equilibrium isotherm, the method may be easily extended to the determination of the complete single-component isotherm.

The column is operated with a mixed carrier containing the adsorbable component (CO_2) and a non-adsorbable gas (Helium) in known proportions, and retention times are measured for small pulses of the adsorbable component at a series of different carrier compositions. There are two ways in which the isotherm may then be found directly by integration: (a) using the moment method; (b) using breakthrough curves.

(a) The chromatographic response peaks obtained are processed and integrated numerically to determine the first and second moments. Information on adsorption equilibrium and kinetics can be obtained through mathematical analysis. The analysis can be accurate only under the conditions of low sorbate concentration, isothermal operation, axially dispersed plug flow regime in the column, instantaneous equilibrium between the sorbate containing carrier gas and adsorbent phases for both concentration and temperature and negligible pressure drop across the packed column. [16]

The mean retention time is a measure of the adsorption equilibrium (Henry's Law constant) while the dispersion of the response peak is determined by the combined effects of mass transfer resistance and axial mixing in the column. By conducting measurements over a range of conditions it is possible to separate the contributions to the peak broadening from mass transfer resistance and axial mixing.

Performing the experiments at low concentrations within the Henry's Law region of the isotherm simplifies the interpretation of the data. In this region of the isotherm, the retention time becomes independent of the size of the sorbate pulse, so changing the pulse size the validity of linearity assumption can be checked. [39]

(b) A breakthrough curve is a plot of the duration of the test against the concentration of the adsorbate in the effluent stream of the carrier-adsorbate gas mixture. Initially, as the gas mixture enters a defined bed filled with zeolites, the adsorbate is adsorbed and the carrier gas passes out of the bed free from the adsorbed gas. This continues as long as the bed of zeolites has capacity to adsorb. When saturation is approached, the gas adsorbed is detected in the effluent gas and its concentration increases until no further adsorption takes place and the composition of the effluent mixture is equal to the composition of the entry mixture.

For an idealized situation, the breakthrough curve is S-shaped, is symmetrical and is described in terms of its (a) midpoint, (b) steepness and (c) shape. The midpoint is a function of the rate of flow of the gas mixture through the bed, the concentration of the adsorbate in the mixture and the capacity of the bed (size and quantity/quality of zeolites in the bed) as well as the operating temperature of the bed. Higher temperatures reduce adsorption capacity and hence reduce retentivity so producing shorter breakthrough times. The steepness of the curve depends on the rate at which the gas mixture passes through the bed. The slower the rate of flow, the steeper the breakthrough curves. Information on adsorption equilibrium and kinetics can then be obtained through mathematical analysis. [40]

Those methods may also be extended to the determination of the binary equilibrium isotherm for a mixture with two adsorbable components but with a different approach to the analysis of the experimental data.

Both chromatographic method offers simplicity and rapidity in producing data, suitability for higher temperature and pressure, applicability in a wider range of diffusivity values and in low sorbate concentration measurements than the conventional static methods. However, the moment method is limited to the low concentration region and it takes much longer time as it requires so many runs to acquire all the points to complete the analysis for a single temperature. Therefore in this work, the gas chromatography method using the breakthrough curve was used exclusively for the determination of the adsorption equilibrium and kinetics of CO_2 in binder-free KY zeolite.

2. THEORY

2.1. Effect of zeolite structural characteristics on CO_2 adsorption

The CO_2 adsorption is influenced by diverse structural characteristics of zeolites including size, polarizing power, distribution, the number of exchangeable cations in their cavities, the size of the pores, and the Si/Al ratio. [14]

2.1.1. Basicity effect on CO_2 Adsorption

The basic properties of zeolites brought by cations allow a strong capitation of acidic molecules by enhancing the electron density of the framework oxygen. The basic strength of these sites increases with the electropositivity of exchangeable cations. [14]

In basicity effect, the diameters of cations are Li^+ (1.4 Å) < Na^+ (1.9 Å) < K^+ (2.7 Å) < Rb^+ (2.9 Å) < Cs^+ (3.3 Å) [59]. Larger cations accept less charge transfer from the neighboring lattice oxygen atoms, these oxygen atoms therefore remain more negatively charged and, hence, more, basic. Therefore, the order of CO_2 adsorption at low pressure follows the same order of basicity of the samples. It is suspected that the basic oxygen atoms play a role in CO_2 adsorption on faujasite Y. The interaction of CO_2 with a cation and a basic oxygen atom would lead to a formation of a bent carbonate-like species. [41]

2.1.2. Si/Al ratio effect on CO_2 Adsorption

Ruthven *et al.* [61, 62] have proven that adsorption capacity and selectivity of zeolites increases when the Si/Al ratio decreases. This effect is more important when the quadrupole moment of molecules is great. This phenomenon could be due to an increase of electric field in the zeolites pores induced by increasing number of charged sites present at the surface of zeolites. Moreover, the basicity of zeolites framework enhances with the content of Al^{3+} ions due to the presence of a greater amount of exchangeable cations. [14]

However, higher silica-alumina ratio is advantageous in some cases as for instance, zeolite KY offers improved catalytic and hydrothermal stability than of KX, it demonstrates more stability under flue gas and adsorption operation conditions, as well as stability in the presence of water vapor. Y zeolites are characterized with less affinity for water than X zeolites, where the affinity

of water is many times higher than CO_2 and therefore the water content will be competing with CO_2 for the sites available for adsorption. Sometimes, the moisture contents of zeolites reach 20% of its own weight. The presence of moisture content significantly decreases adsorption capacity of cationic zeolites by favoring the formation of bicarbonates and decreasing strength and heterogeneity of the electric field. [42]

2.1.3. Polarization, distribution, number and size of exchangeable cations effect on CO_2 Adsorption

The polarizing power of the exchangeable cations represents a very important factor that influences the local electric field and the polarization of the CO_2 molecules on the zeolites. The polarization of CO_2 induced by the electric field of the cation causes a shift to higher frequencies. The shift is expected to increase with decreasing cation radius. [14] Therefore the polarity of the cations can be written inversely proportion to the ionic radius: $Li^+ > Na^+ > K^+ > Rb^+ > Cs^+$. Having said that, the polarizing power is not the main factor that governs the adsorption of CO_2 because in Pirngruber's *et al.* study [41], it was discovered that the less polarizing cations Cs+ and K+ adsorb more strongly CO_2 than Na+ and Li+. The authors identified two possible explanations for the strong interaction of CO_2 with CsY and KY: (i) the formation of bridged adsorption complexes where CO_2 simultaneously interacts with two cations and (ii) an adsorption mode where CO_2 simultaneously interacts with the cation and lattice oxygen atoms.

Therefore, other factors should be considered before drawing conclusions on the CO_2 adsorption due to the polarizing power.

The number of cations which are able to interact with adsorbates have also an importance in the adsorption process. Indeed, a calorimetric study by Khvoshchev and Zverev [43] of CO_2 adsorption in faujasites CaY and CaX has indicated that the isosteric heat of CO_2 adsorption on the zeolite CaX is higher than that of CO_2 on the zeolite CaY. This could be a consequence of a higher CO_2 adsorption on zeolite CaX than on the zeolite CaY. Moreover, this difference could also be due to a greater number of Ca^{2+} cations in the zeolite CaX which are able to interact directly with the adsorbed CO_2 molecules, than in zeolite CaY. Additionally, the distribution plays an important role as it can bring this heterogeneous character of the CO_2 adsorption. [14]

The pore sizes of the zeolites can also influence the capacity and rate of CO_2 adsorption. The presence of small exchangeable cations that can penetrate more easily within the zeolites

cavities will have stronger interaction with CO_2 as the big cations and therefore will increase the adsorption. The relationship between the CO_2 adsorption capacity of zeolites and the size of their pores depends particularly of the pressure (loading). Indeed, at low pressures, the density of the adsorbate is highest in the smaller pores while that is higher in larger pores at high pressures. This was proven by Barrer [44] as he indicated that the affinity of the zeolite NaA for CO_2 is higher than that of zeolites NaX and NaY at low pressures, this was due to a small diameter of zeolite A.

2.1.4. Importance of cation exchange in the performance of the zeolite on CO_2 Adsorption

It is shown in Khelifa's *et al.* studies [45, 46], that the CO_2 adsorption affinity decrease when Na^+ cations of an X-type zeolite are exchanged by the M^{2+} cations (Mg^{2+}, Sr^{2+}, Zn^{2+} , Cu^{2+}). However, there is an increase of the CO_2 adsorption affinity when the degree of Na^+ exchange increases. It is also shown that the CO_2 adsorption on zeolites X exchanged with Ni^{2+} and Cr^{3+} decreases as compared to that of zeolite NaX due to a decrease of the adsorbate-adsorbent interaction. This phenomenon has been associated with a depopulation of sites III (Figure 2) and a decrease of electric field in the cavities of zeolite. [14]

Nevertheless, Kiselev *et al.* [46] studied the adsorption properties of zeolites MgNaX and CaNaX, he showed that the substitution of Na^+ cations by Mg^{2+} and Ca^{2+} cations changes only the CO_2 adsorption when the rate of exchange is superior to 40-50%.

A similar effect has also been observed by Khvoshchev and Zverev [43] in their calorimetric study where the isosteric heat of CO_2 adsorption on the dehydrated faujasites (Mg, Ca)-X and (Mg, Ca)-Y was examined, following the substitution of a part of the Ca^{2+} ions by the Mg^{2+} ions. The decrease of heat of adsorption achieved during the substitution has been attributed to a greater screening of Mg^{2+} ions by the oxygen atoms electric field of zeolites and therefore, do not form adsorption complexes with CO_2 as compared to that of Ca^{2+} ions. This might be caused by the penetration of Mg^{2+} ions deep within six-membered rings of the framework or to their localization principally outside the cavities of zeolites. [14]

They have also shown that Ca^{2+} ions located in large cavities of faujasites are preferential adsorption centers for CO_2. The heats of adsorption in the ranges of coverages corresponding to the interactions of adsorbed molecules with such ions are higher than those for sodium zeolites. Therefore, the substitution of Na^+ by Ca^+ in zeolites leads to an increase of CO_2 adsorption heats at low coverages. [43]

2.2. Adsorption Equilibrium Loading Measurement by Chromatographic Breakthrough Experiments

In chromatographic breakthrough experiments, the dynamic equilibrium loading can be obtained by integrating the molar flow profiles of the breakthrough curves by the following equation [48]:

$$q_i = \frac{1}{m_{ads}}\left(F_{f,i}t_n - \int_0^{t_\infty} F_i dt - \varepsilon_b V_c C_{i0}\right) \quad (1)$$

where m_{ads} is the adsorbent mass, $F_{f,i}$ is the feed molar flow rate of component i at the inlet of the bed; F_i is the molar flow rate of component i at the outlet of the bed, t_n is the saturation time, ε_b is the bed porosity, V_c is the column adsorption volume, and C_{i0} is the feed gas-phase concentration at the inlet of the fixed bed.

2.3. Adsorption Equilibrium Isotherm Models

2.3.1. Langmuir Model

The Langmuir equation has been widely applied to estimate the adsorption equilibrium of single gases owing to its simplicity with only two parameters and sufficient accuracy for various adsorbents. [49]

It is based on the four following assumptions [48]:

1. The absorbent surface is homogeneous and the energy of all adsorption sites are equal.
2. The interaction between the adsorbate particles could be neglected.
3. Each site can only hold one adsorbate molecule.
4. Adsorption equilibrium is dynamic, and the adsorption rate is equal to that of desorption from the surface.

The Langmuir model for a single component can be represented by the following equation [64]:

$$q = q_M \frac{bp}{1 + bp} \quad (2)$$

where q is the adsorbed concentration at equilibrium; q_M is the specific adsorbed saturation capacity; p is the partial pressure and b is the adsorption affinity constant of the Langmuir isotherm, which indicates the attraction force between the adsorbate molecule onto the surface of the adsorbent.

The effect of temperature on the adsorption affinity constant b , is taken into account by the integrated van't Hoff equation:

$$b = b_\infty e^{(-\Delta H/RT)} \tag{3}$$

where b_∞ is the pre-exponential factor of the affinity constant at an infinite temperature, R is the ideal gas constant, $-\Delta H$ is the heat of adsorption, and T is the experimental temperature. As the adsorption is an exothermic process, the b constant decreases by increasing temperature.

2.3.2. Dual-site Langmuir Model

In the dual-site Langmuir model (DSL), the adsorbable species are distributed in two sites, each one following the Langmuir model assumptions, with different binding energies and maximum adsorption capacity in each site. The dual-site Langmuir model for a single component can be represented by the following equation [50]:

$$q = q_{m1}\frac{b_1 p}{1 + b_1 p_i} + q_{m2}\frac{b_2 p}{1 + b_2 p} \tag{4}$$

where q_{m1} and q_{m2} are the maximum adsorbed concentrations of site 1 and 2, respectively; b_1 and b_2 are the adsorption affinity constants in each site. This model deviates from the ideal Langmuir model accounting for certain heterogeneity of adsorbent surface. It reverts to the Langmuir model (Eq. 2) if we consider only one site.

The extended DSL model isotherm to multicomponent systems (component i and j) is given by the following equation:

$$q_i = q_{m1,i}\frac{b_{1,i}\, p_i}{1 + \sum_{j=1}^{n} b_{1j} p_j} + q_{m2,i}\frac{b_{2,i}\, p_i}{1 + \sum_{j=1}^{n} b_{2j} p_j} \tag{5}$$

The evolution of the heats of adsorption as function of coverage depends on the contribution of adsorbate-adsorbent interactions, which either remain constant or decrease. [41] The isosteric heat (ΔH_{st}) is the heat of adsorption as a function of the amount adsorbed and it is defined by the following equation [44]:

$$\frac{\Delta H_{st}}{RT^2} = -\left(\frac{\partial \ln p}{\partial T}\right)_q \tag{6}$$

Assuming ΔH_{st} is independent of the temperature, the isosteric heat can be calculated directly by integrating equation 6 at a fixed coverage from experimentally measured adsorption isotherms in a plot of $\ln p$ against $1/T$ [17]:

$$\ln p = constant - \frac{\Delta H_{st}}{RT} \tag{7}$$

The evolution of the heat of adsorption as a function of loading depends on the intermolecular adsorbent-adsorbate molecular interactions. Higher values of isosteric heats means stronger interactions. It can also give us an idea on the heterogeneous behavior of the material. [63]. It is fair to say that the isosteric heat of sorption of CO_2 on zeolites A, X and Y deceases with increasing coverage. [65] This behavior can be predicted or calculated numerically by the differentiation of the DSL model (eq. 4), assuming constant loading ($dq = 0$), and substituting the result in the isosteric heat equation (eq. 6), resulting in the following equation [48, 51]:

$$(-\Delta H_{st}) = \frac{q_{m1}\dfrac{b_1 \Delta H_1}{(1+b_1 p)^2} + q_{m2}\dfrac{b_2 \Delta H_2}{(1+b_2 p)^2}}{q_{m1}\dfrac{b_1}{(1+b_1 p)^2} + q_{m2}\dfrac{b_2}{(1+b_2 p)^2}} \tag{8}$$

It is therefore a numerical solution (eq.8) that can be used to predict the increase or decrease of the isosteric heat with loading depending on the heterogeneity of the adsorbent. In the limit, the value is constant when the surface adsorption in both sites are the same, meaning they are homogeneous, as assumed in the Langmuir model. [51].

2.4. Adsorbent Screening Metrics

After measuring both CO_2 and N_2 isotherms, adsorbent screening is usually performed based on the so-called "adsorbent metrics" that can be calculated using single-component isotherms. Selectivity and the working capacity using the pure component isotherms at a given feed condition have been suggested as adsorbent metrics by Tezel [52]. Other metrics such as pure-component and competitive selectivity, Henry's selectivity, and others are found in literature [53, 54, 55] and are used to evaluate the separation performance.

The selectivity (α) of CO_2 over N_2 can be defined as:

$$\alpha = \frac{q_{CO2}/q_{N_2}}{p_{CO2}/p_{N_2}} \tag{9}$$

where q_{CO2} is the equilibrium adsorption quantity of CO_2 and q_{N_2} is that of N_2 at the same pressure and temperature. p_{CO2} and p_{N_2} are the partial pressures of CO_2 and N_2 respectively.

The Henry selectivity (α_H) is calculated at low concentrations, where the adsorption isotherm is in the limit of the linear range. It is defined by the following equation [54]:

$$\alpha_H = \frac{H_{CO_2}}{H_{N_2}} = \frac{(q_{m1}b_1 + q_{m2}b_2)_{CO_2}}{(q_{m1}b_1 + q_{m2}b_2)_{N_2}} \tag{10}$$

where q_{m1} and q_{m2} are the saturation concentrations for site 1 and site 2, respectively. b_1 and b_2 are the adsorption affinity constants in each site.

Pure component selectivities (α_P) can be calculated by Eq. 11 and competitive (multicomponent) selectivites (α_C) by Eq.12 where y_{CO_2} and y_{N_2} represent the feed molar fraction of CO_2 and N_2 [53].

$$\alpha_P = \left|\left(\frac{q_{CO_2,pure}}{q_{N_2,pure}}\right)\frac{y_{N2}}{y_{CO_2}}\right|_{feed} \tag{11}$$

$$\alpha_C = \left|\left(\frac{q_{CO_2,comp}}{q_{N_2,comp}}\right)\frac{y_{N2}}{y_{CO_2}}\right|_{feed} \tag{12}$$

The working capacity of an adsorbent is defined as the difference in equilibrium capacities between the high and low pressures for the case of PSA/VSA and from high and low temperature in the case of TSA. A general expression including both temperature and pressure for the pure and competitive working capacity is shown below [56]:

$$\beta_P = |(q(T1, P1) - q(T2, P2)\ |_{pure} \quad (13)$$

$$\beta_C = |(q(T1, P1) - q(T2, P2))\ |_{comp} \quad (14)$$

where $q(T1, P1)$ is the CO_2 adsorption amount at temperature T1 and partial pressure P1 in the adsorption step, and $q(T2, P2)$ is that of temperature T2 and regenerating pressure P2 in the desorption step.

3. EXPERIMENTAL STUDIES

3.1. Breakthrough Experimental Apparatus

A single and multi-component breakthrough apparatus has been used to study the fixed bed adsorption kinetics of CO_2 and N_2 in their binary mixtures in KY zeolite. The experimental system mainly consists of three sections:

a) Gas preparation system. b) Adsorption column. c) Gas Analysis (TCD).

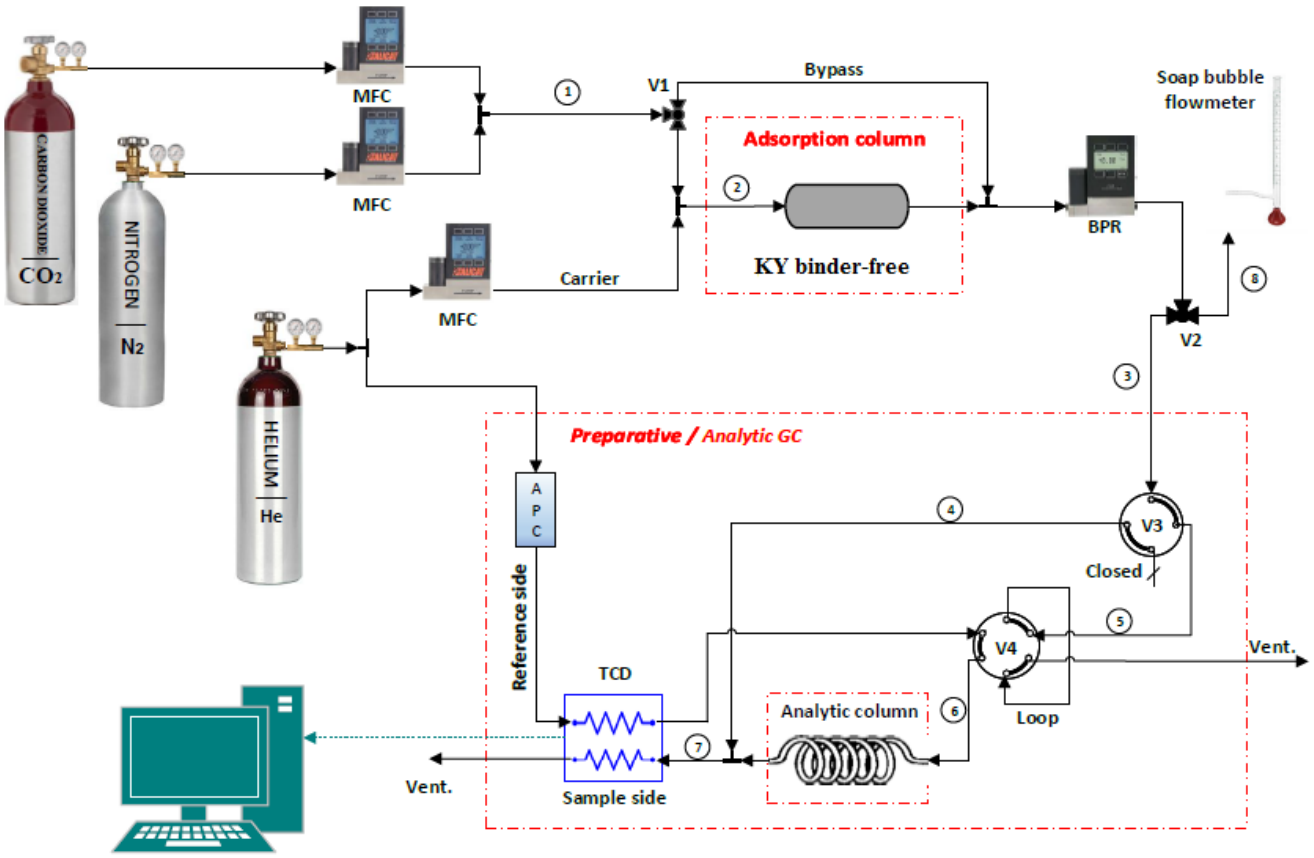

Figure 5: Schematic drawing of the experimental set-up used to perform single- and multi-component breakthrough experiments to measure the adsorption equilibrium.

Figure 5 shows the apparatus schematic used to perform the experiment. In the gas preparation section, helium is used as a carrier gas as it enters the system through the carrier stream. The adsorbate gas (CO_2 or N_2 or both species) goes into the system through line 1. The carrier-gas is sent directly to the column to keep the material clean and the adsorbate gas first is bypassing the column to verify the flowrate. When valve V1 is switched, the adsorbable species joins with the carrier gas and go to the column oven through line 2. Helium is also connected directly to the TCD to be used as reference.

Mass flow controllers (MFC) are used to set the flow rates and the total volumetric flow rate is measured using the bubble flow meter technique, which is done by sending the gas mixture into the bypass stream (using V1) and then into the ventilator (using V2) where the bubble flow meter, equipped with EC sensors, is located. Back pressure controller (BPC) is used to set the total pressure of the system.

This apparatus is designed to perform single and multi-component experiments, with the VICI Valco four-way valve (V3) used to select the type of the experiment. The configuration presented in Figure 5 is selected to perform a multi-component experiment, where the gas exiting the adsorption column is sent to the VICI Valco six-way valve (V4) so that the stream can pass by the loop, and then either go to ventilation or through line 6, as the carrier gas exiting the reference side of the TCD enters the valve and drags the sample contained within the loop to the analytic section. In the analytic section, line 6 goes to the chromatographic column (Supelco silica gel 3”), with the effluent being detected in the sample side of the TCD.

To perform a single-component experiment, valve V1 must be in the opposite position so that the output gas of the adsorption column bypasses valve V2 and go directly to the sample side of the TCD through line 4.

The fixed bed adsorption column is filled with binder-free KY zeolites. Table 2 shows the properties of the adsorption column, adsorbent and operating conditions. The adsorbate and inert gases were supplied by Air Liquide with the following purities: He ALPHAGAZ 2 (99.9998 %), CO_2 N48 (99.998%) and nitrogen N50 (99.999%).

Table 2: Column, Adsorbent and Operating Conditions.

Parameter	Value
Adsorbent properties	
Total weight	26.2 g
Beads diameter	1.60 -2.50 mm
Column properties	
Bed density	0.649 g/cm^3
Bed porosity	0.4
Column Length	6.46 cm
Column Internal Diameter (I.D)	2.82 cm
Cross-Sectional Area	6.24 cm^2
Volume	40.3 cm^3
Fluid properties	
Pressure	1.00 – 3.50 bar
Temperature	313 – 423 K

3.2. Experimental Procedures

Before the first run, the adsorption column is activated for 12 hours at 623 K under vacuum and pure helium flows (10 mL/min). This activation step under high temperature and vacuum is critical to remove the any pre-absorbed components, such as water. The weight of the column before and after the activation was noted to define the amount of dehydrated water.

To prepare the gases, the flow rates of both carrier gas (He) and adsorbate gases (CO_2/N_2) are adjusted using the mass flow controller (MFC) so that the desired partial pressure is achieved when both gases are mixed. The total pressure is set and taken into account using the back pressure controller (BPC).

Before sending the prepared mixture into the adsorption column, it is best to keep using the bypass (V1) and then only switching valve (V2) to the TCD side so that the concentrations of the carrier gas and the adsorbate are monitored before going into the adsorption column. This gives an idea of how the curve should look like after the adsorption is complete. The next step is to switch valve (V1) to the bed-side, and therefore the mixture passes through the adsorption column, which is placed inside a temperature controlled oven. For the first set of runs, the temperature was set at 313 K.

The mixture then exits the column and enter the thermal conductivity detector (TCD) which provides an electronic signal proportional to the concentration of gases. Initially, as the gas mixture enters, the adsorbate is adsorbed and the carrier gas passes out of the bed free from the adsorbed gas. This continues as long as the bed of zeolites has capacity to adsorb. When saturation is approached, the gas adsorbed is detected in the effluent gas and its concentration increases until no further adsorption takes place and the composition of the effluent mixture is equal to the composition of the entry mixture. The curve, which looks similar to an S-shape, is collected and transferred into data to be able to perform mathematical analysis on the adsorption that took place.

This experiment was repeated with different partial pressures at the following temperatures: 313 K, 373 K, 423 K. Before each run, the column had to be re-activated under high temperature (around 523 K) for at least 30 minutes with pure He flow, to remove any carbonate species formed from the previous run. After a few set of runs is completed, the column is activated overnight (12 hours at 523K) to make sure that the zeolite is clean and ready for adsorption in the next day.

3.3. Commercial binder-free Zeolite KY

The sample of the commercial binder-free zeolite KY studied in this work, was furnished and supplied as 1.6-2.5 mm beads by Chemiewerk Bas Kostritz GmbH (Germany). Cation exchange of a parent NaY sample with a Si/Al ratio of 2.5 was performed to achieve the composition of 95% K^+. Table 3 shows some of the textural properties of the adsorbent used in the experimental studies. Detailed information is given in Appendix B.

Table 3: Textural properties of the binder-free KY zeolite studied in this work.

Adsorbent Type	**KY zeolite**
BET surface area (S_{Bet})	570 m^2 g^{-1}
Langmuir surface area ($S_{Langmuir}$)	845 m^2 g^{-1}
External surface area (S_{ext})	13.0 m^2 g^{-1}
Micropore surface area (S_{mic})	557 m^2 g^{-1}
Micropore volume (V_{mic})	297 mm^3 g^{-1}
Average pore width (W_{mic})	2.10 nm
Total Pore Volume (V_{Total})	316 mm^3 g^{-1}

4. RESULTS AND DISCUSSION

4.1. Adsorption Equilibrium of CO_2 on binder-free KY

The single component adsorption equilibrium data of CO_2 in binder-free KY was collected at three temperatures, 313, 373, 423 K, and pressures up to 3.5 bar. The experimental conditions of all performed runs, including flow rates of adsorbates (CO_2) and inert gas (helium), partial pressures of adsorbate, and total pressure of the process, are reported in Table 4.

From the breakthrough data, the amount adsorbed of each run was determined directly from the fixed bed breakthrough experiments using equation (1) as shown in Appendix A. The calculated loadings after the dead volume correction are shown in Table 4. Plotting the uptake capacity (loading) over the partial pressure will provide us the adsorption isotherms of CO_2 on binder-free zeolite KY, which are illustrated in Figure 6.

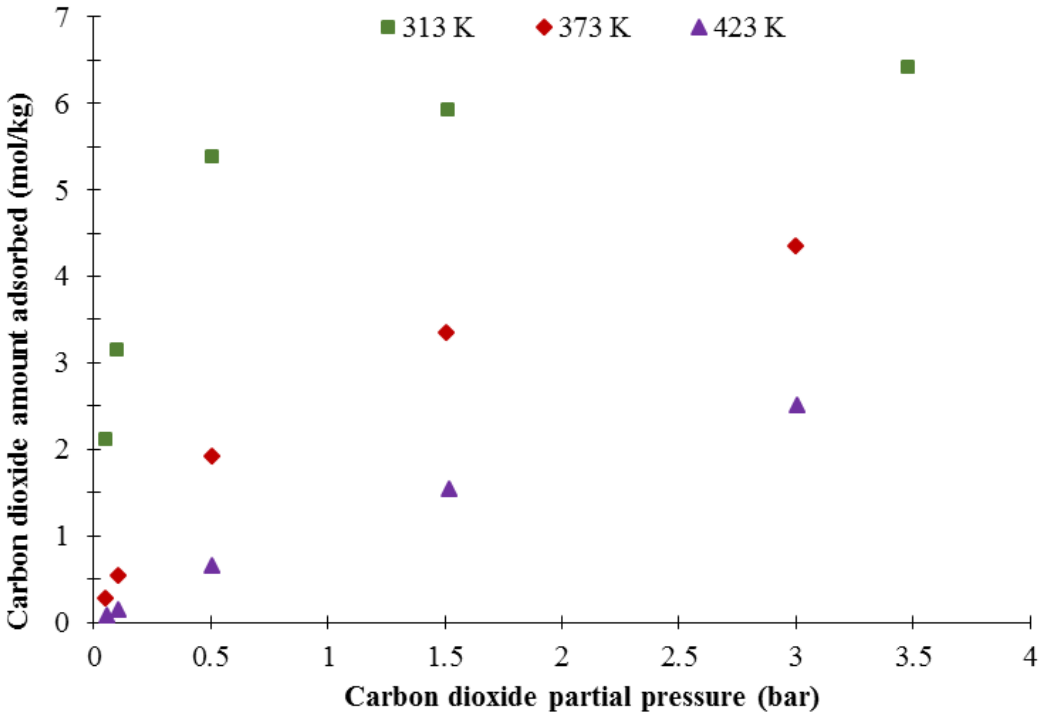

Figure 6: Adsorption equilibrium isotherms of CO_2 on zeolite KY.

Table 4: Experimental conditions of all runs at 313, 373 and 423 K to study the CO_2 adsorption on binder-free KY zeolite.

RUNS (313K)	**CO_2 Flow (ml/min)**	**He Flow (ml/min)**	**Total Pressure (bar)**	**CO_2 partial pressure (bar)**	**Loading (mol/kg)**
1.1	4.61	87.6	1	0.05	2.12
1.2	9.22	83.0	1	0.1	3.16
1.3	46.1	46.1	1	0.5	5.38
1.4	27.7	64.5	5	1.5	5.92
1.5	64.5	27.7	5	3.5	6.42
RUNS (373K)	**CO_2 Flow (ml/min)**	**He Flow (ml/min)**	**Total Pressure (bar)**	**CO_2 partial pressure (bar)**	**Loading (mol/kg)**
2.1	3.87	73.5	1	0.05	0.275
2.2	7.74	69.6	1	0.1	0.543
2.3	38.7	38.7	1	0.5	1.92
2.4	23.2	54.2	5	1.5	3.36
2.5	46.4	30.9	5	3.0	4.46
RUNS (423K)	**CO_2 Flow (ml/min)**	**He Flow (ml/min)**	**Total Pressure (bar)**	**CO_2 partial pressure (bar)**	**Loading (mol/kg)**
3.1	3.41	64.8	1	0.05	0.0814
3.2	6.82	61.4	1	0.1	0.149
3.3	34.1	34.1	1	0.5	0.655
3.4	20.5	47.8	5	1.5	1.54
3.5	40.9	27.3	5	3.0	2.51

As can be seen, the amount adsorbed of CO_2 in zeolite KY increases by enhancing the partial pressure. At a fixed pressure, the adsorption capacity decreases when the temperature is increased in accordance to the exothermic behavior of the adsorption process.

The isotherms were firstly modeled by a numerical procedure in order to minimize the absolute difference (Δq) between the experimental values (q) and the predicted or calculated values (q_{cal}) on all experimental runs (M) by applying the Langmuir model (eq. 2). Therefore, the objective is to minimize the following equation:

$$\Delta q = \sum_{i=1}^{M} (q_{cal} - q)^2 \tag{15}$$

Following the minimizing procedure (eq.15), values of the Langmuir model parameters q_m, b and ΔH can be determined. The coefficient of determination r^2 represents the percentage of variability in the dependent variable, meaning that it is employed to analyze the fitting degree of the isotherm with the experimental data. It is a value that varies from 0 to 1, closer the coefficient to 1 means less percentage of error. It is calculated by the following equation [50]:

$$r^2 = \frac{(q - \overline{q_{cal}})^2}{\sum(q - \overline{q_{cal}})^2 + (q - q_{cal})^2} \tag{16}$$

Table 5 shows the calculated model parameters along with the coefficient of determination when the Langmuir model was applied to the experimental isotherms. The adsorption equilibrium isotherm of CO_2 on binder-free KY zeolite by applying the Langmuir model is shown in Figure 7.

Table 5: Adsorption equilibrium Langmuir model parameters for CO_2 on binder-free KY zeolite.

q_m (mol.kg)	b * (bar^{-1})	$-\Delta H$ (kJ/mol)	r^2 (-)
6.43	9.66	39.4	0.997

** The reference temperature used is 313.15 K*

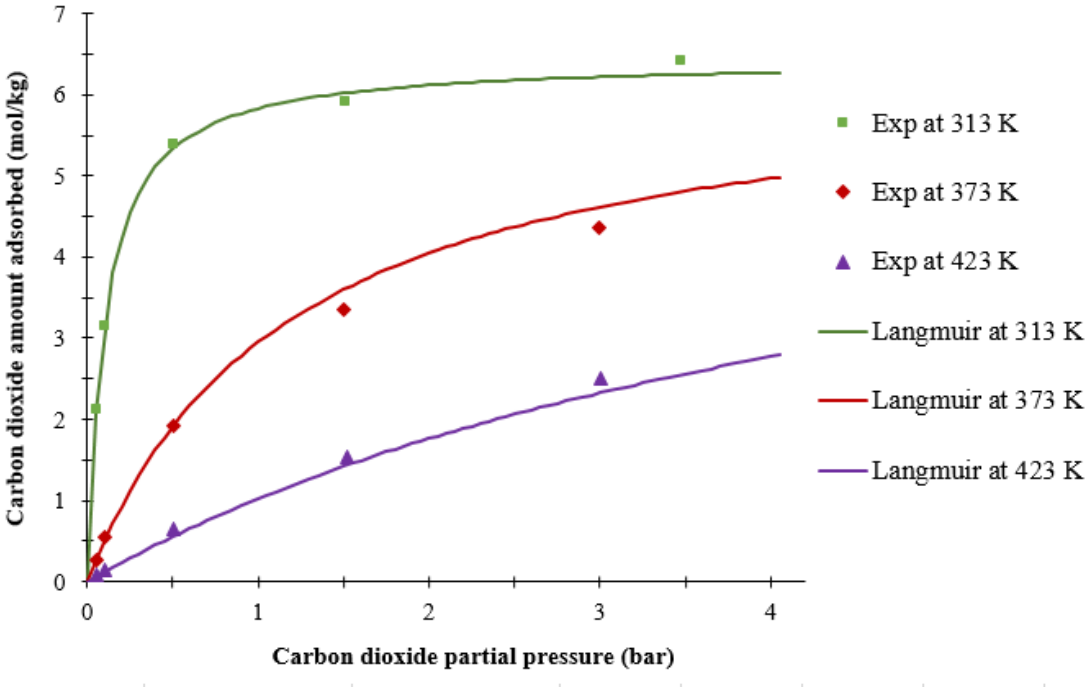

Figure 7: Adsorption equilibrium isotherm of CO_2 on binder-free KY zeolite and fitting with the Langmuir model.

The Langmuir model is simple and reasonably accurate, however it assumes that the sites are homogenous and so the surface adsorption is equal in all sites. This assumption can only be correct if the isosteric heat as a function of the capacity coverage, is constant. Therefore, a plot of the isosteric heat over the coverage is necessary to find out if the Langmuir model is thermodynamically consistent with experimental data.

As mentioned before, the isosteric heat can be calculated directly by integrating equation (6) at a fixed coverage from experimentally measured adsorption isotherms in a plot of $\ln p$ against $1/T$. Therefore, using equation (7), values of the isosteric heat can be determined from the slope as shown below in Figure 8.

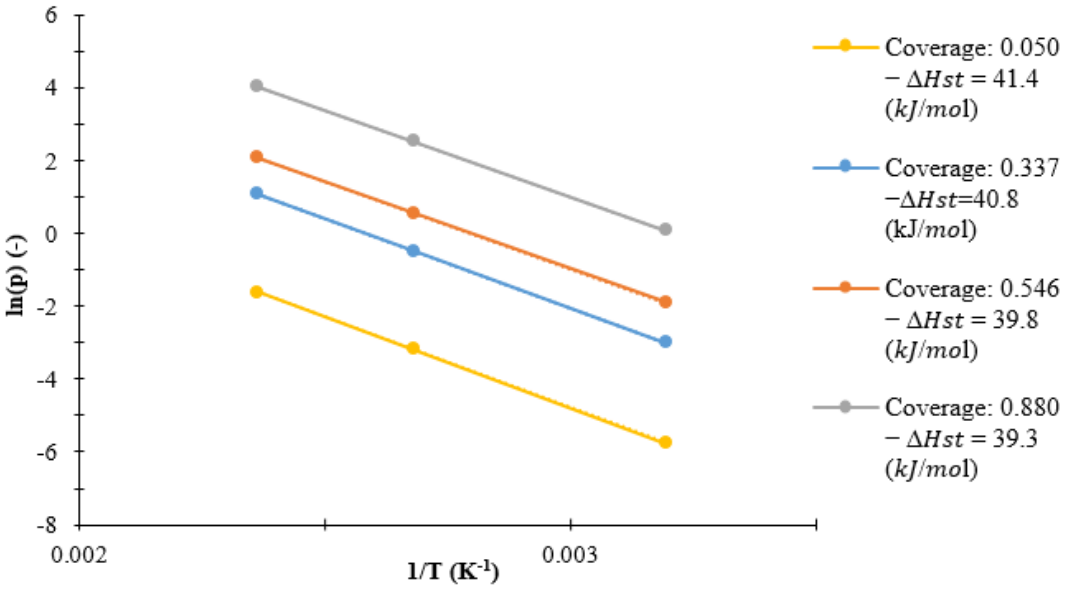

Figure 8: Plot of ln p over 1/T at fixed coverages for calculating the isosteric heat of CO_2.

As can be seen, the slope of the isosteric heat decreases as a function of coverage. This verifies the fact that the surface adsorption in the sites are heterogeneous, this can be explained by the charge density in the zeolite that interact with the strong quadrupole moment of the CO_2 molecule, giving rise to the heterogeneous surface. Additionally, Pirngruber *et al.* [41] have shown that K+–K+ distances inside the supercage of zeolite KY are smaller than NaY (the order of 8.6 A˚). This small distance allows the interaction of CO_2 with two K+ located in different sites (K+...O=C=O...K+) of supercage resulting in different energy of adsorption. Also, the authors conclude that a dual-site adsorption mode seems to be possible.

Using the DSL model (eq.4) and the same numerical procedure (minimizing eq. 15), the fitting is shown in Figure 9. Table 6 shows the calculated DSL model parameters for both sites.

Table 6: Adsorption equilibrium DSL model parameters for CO_2 on binder-free KY zeolite.

q_m (mol/kg)		$b*$ (bar^{-1})		$-\Delta H$ (kJ/mol)		r^2 (-)
q_{m_1}	q_{m_2}	b_1	b_2	$-\Delta H_1$	$-\Delta H_2$	
3.93	2.80	4.98	18.0	38.3	42.6	0.996

** The reference temperature used is 313.15 K*

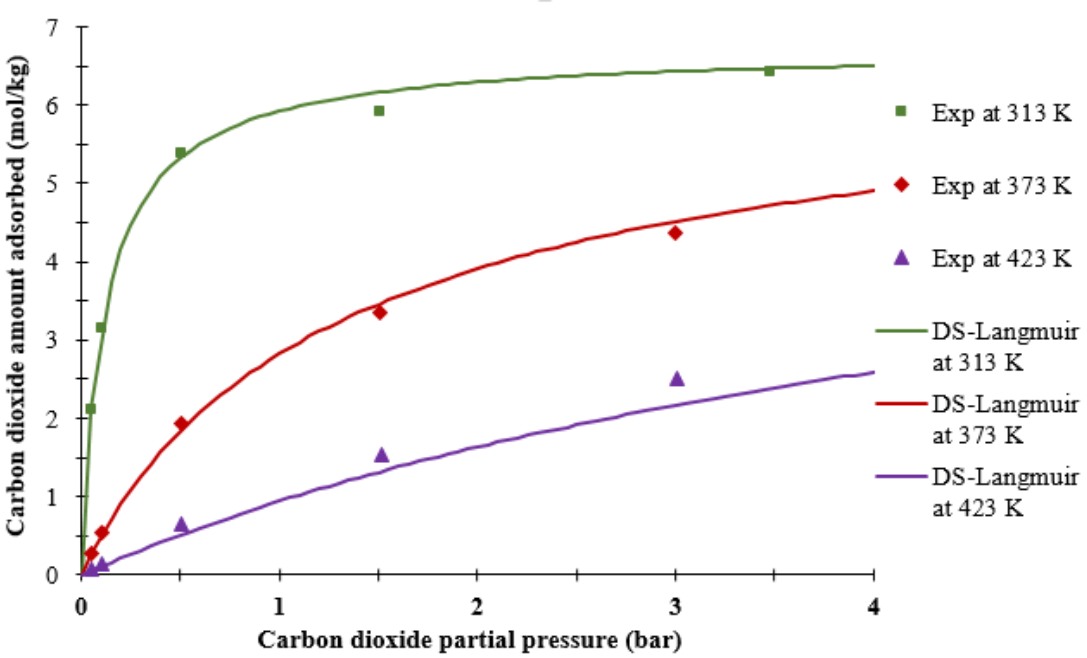

Figure 9: Adsorption equilibrium isotherms of CO_2 on binder-free KY zeolite and fitting using the DSL model.

The isosteric heat can be predicted or numerically calculated using equation (8). Figure 10 shows the numerical isosteric heat along with the previously calculated experimental values as a function of coverage, where it can be seen that the DSL model predicts the experimental observation of the slight decrease of the net isosteric heat of CO_2 as a function of coverage indicating a heterogeneity energy surface.

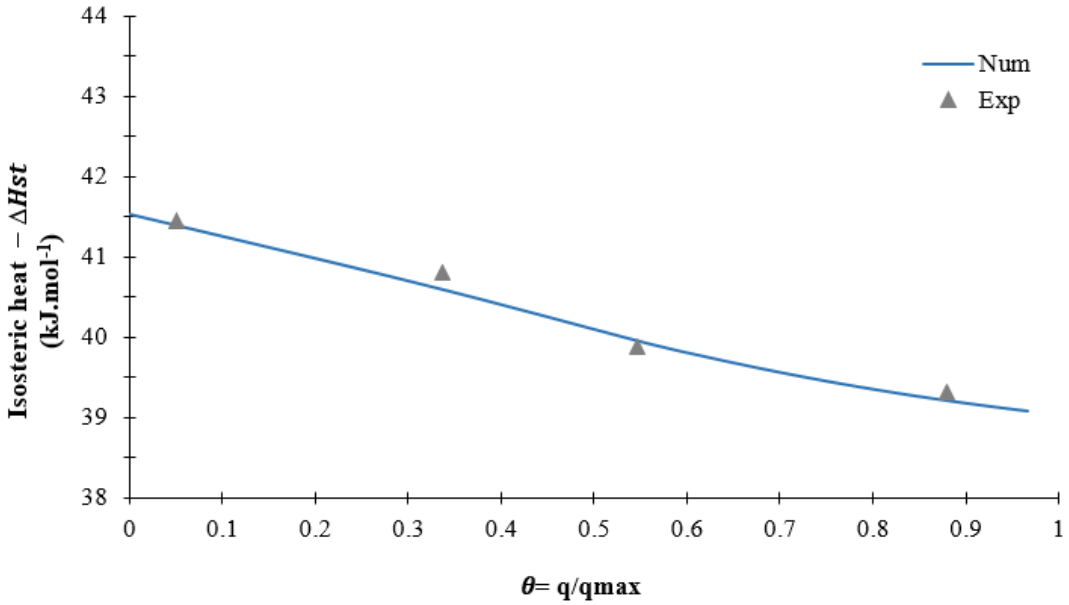

Figure 10: Isosteric heat of adsorption as a function of CO_2 coverage experimental and numerically predicted by the DSL model in binder-free zeolite KY.

4.2. Comparison of CO_2 adsorption equilibrium data in different ion-exchanged zeolites

Figure 11 show a comparison of the isotherms collected in this work for binder-free zeolite KY and other Y zeolites modified by alkali metal cation exchange (NaY, LiY, KY, CsY) collected at 323 K, shown in literature [41] where units were converted from molecules/UC into mol/kg. The isosteric heats are also compared and shown in Figure 12.

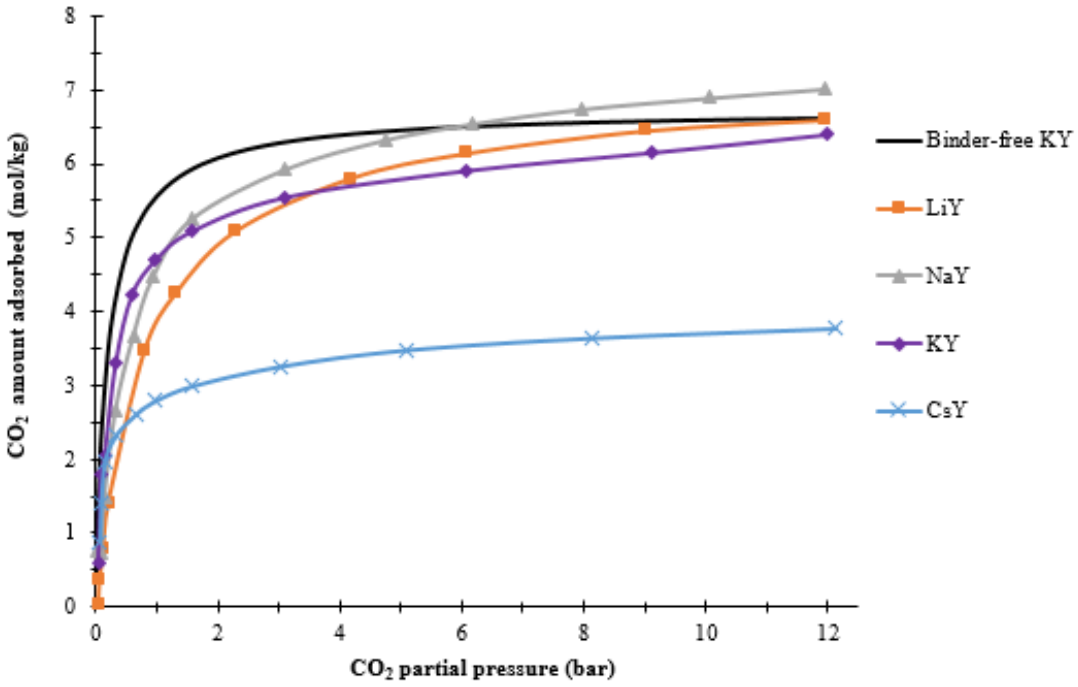

Figure 11: Comparison of CO_2 adsorption isotherms in different ion-exchanged zeolites at 323 K [41].
*The data for binder-free KY was measured in this work.

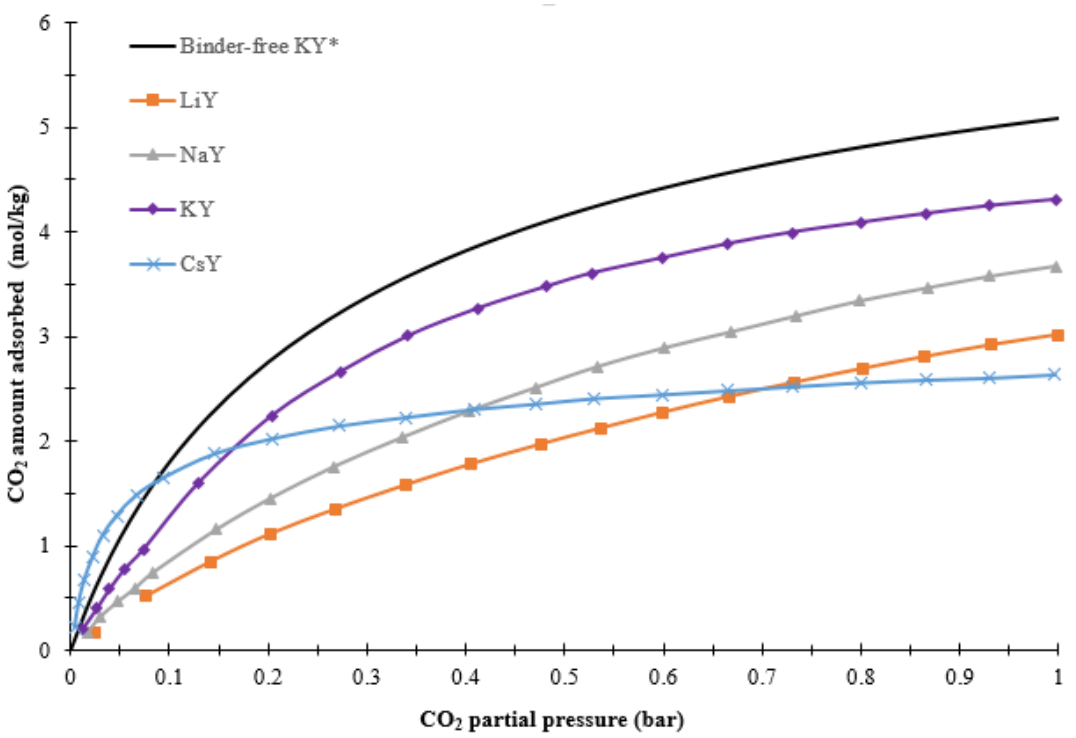

Figure 12: Comparison of adsorption isotherms in low pressure region at 333 K on cation exchanged zeolites Y. [41]

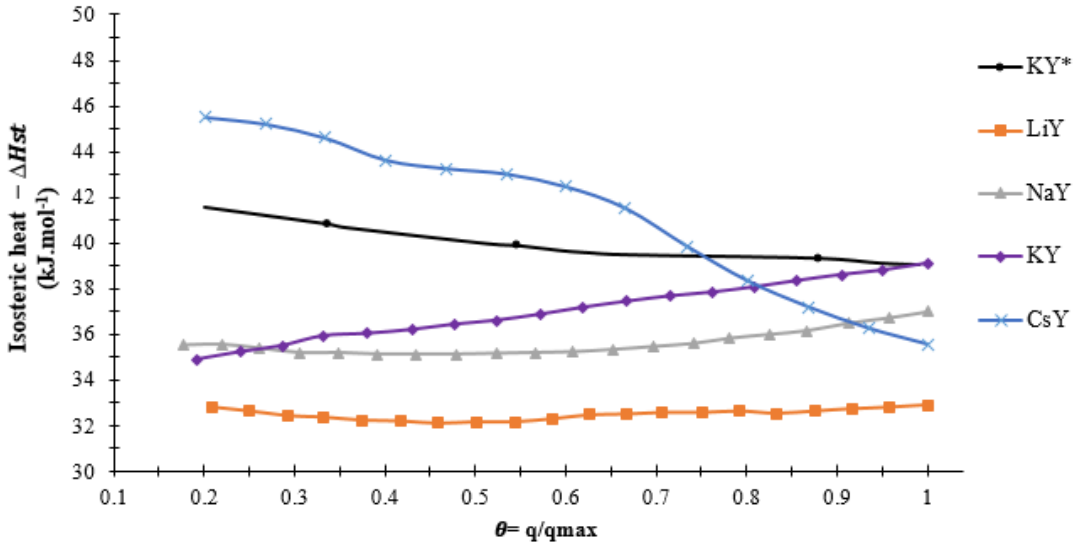

Figure 13: Isosteric Heat Comparison of CO_2 on alkali-metal exchanged FAU zeolites [41].
* The data for binder-free KY was measured in this work.

As be seen, the adsorption capacity of CO_2 in binder-free KY is very competitive comparing it to most of the studied alkali metal exchanged zeolites. At low pressures, it is visible that binder-free KY demonstrates the highest loading, this is confirmed in Figure 12 where the adsorption isotherms are studied in the low pressure region at 333 K. In agreement with the results of Pirngruber *et al.* [41], a clear trend in the order of adsorption at low pressure is observed: LiY < NaY < CsY < KY. The K and Cs forms have more strongly concave downward isotherms compared to the almost linear isotherms for NaY and LiY. This indicates a responsiveness of acidic CO_2 to the basic properties of the zeolites containing larger cations, as Walton *et al.* [20] indicated.

Also, since the material studied in this work is binder-free, meaning that the non-zeolitic components (temporary binder) was converted to zeolite during a hydrothermal conversion after the manufacturing procedure, binder-free KY should have up to 20% increased capacity [24-26, 18]. This is visible in all comparisons as binder-free KY form follows the same trend as KY but with around 10 - 20 % increased capacity.

For partial pressures above 6 bar at 323 K, NaY is characterized with the highest adsorption capacity followed by binder-free KY, then LiY and KY and finally CsY, as shown in Figure 11. These trends are explained by the volume occupied by the cations, which reduces the space available for adsorption of CO_2 when the pores are reaching saturation [41]. It is also explained by the basicity effect, the basic strength of the sites increases with the electropositivity of exchangeable cations and since larger cations accept less charge transfer from the neighboring lattice oxygen atoms, these oxygen atoms therefore remain more negatively charged and so the sites become less basic, hence, the adsorption capacity decreases [14]. Therefore, the trend in the order of adsorption at intermediate and high pressure is as follows: NaY $\sim$ Binder-free KY $>$ LiY $\sim$ KY $>$ CsY.

Some could say that LiY should have much higher adsorption capacity than KY since it is nearly half its size (0.68 Å radius for Li^+ and 1.33 Å for K^+). However, the large cavities in faujastie-type zeolites makes it easy for K^+ ions to become a competitive adsorption center for CO_2. As shown in Figure 13, the heats of adsorption demonstrating the interactions of adsorbed molecules with such ions are higher than those for lithium as well as the sodium zeolites.

Further isotherms and isosteric heats comparisons of binder-free KY and other ion-exchanged zeolites on the adsorption of CO_2 are presented in Appendix C.

4.3. Adsorption equilibrium of N_2 on binder-free KY

The single component adsorption equilibrium data of N_2 in binder-free KY was collected at three temperatures, 313, 373, 423 K, and for pressures up to 3.5 bar. The experimental conditions of all performed runs, including flow rates of adsorbates (N_2) and inert gas (helium), partial pressures of adsorbate, and total pressure of the process, are reported in Table 7.

From the breakthrough data, the amount adsorbed of each run was determined directly from the fixed bed breakthrough experiments using equation (1) as shown in Appendix A. The calculated loadings after the dead volume correction are plotted over the partial pressure to provide the adsorption isotherms of N_2 on binder-free zeolite KY, as illustrated in Figure 14.

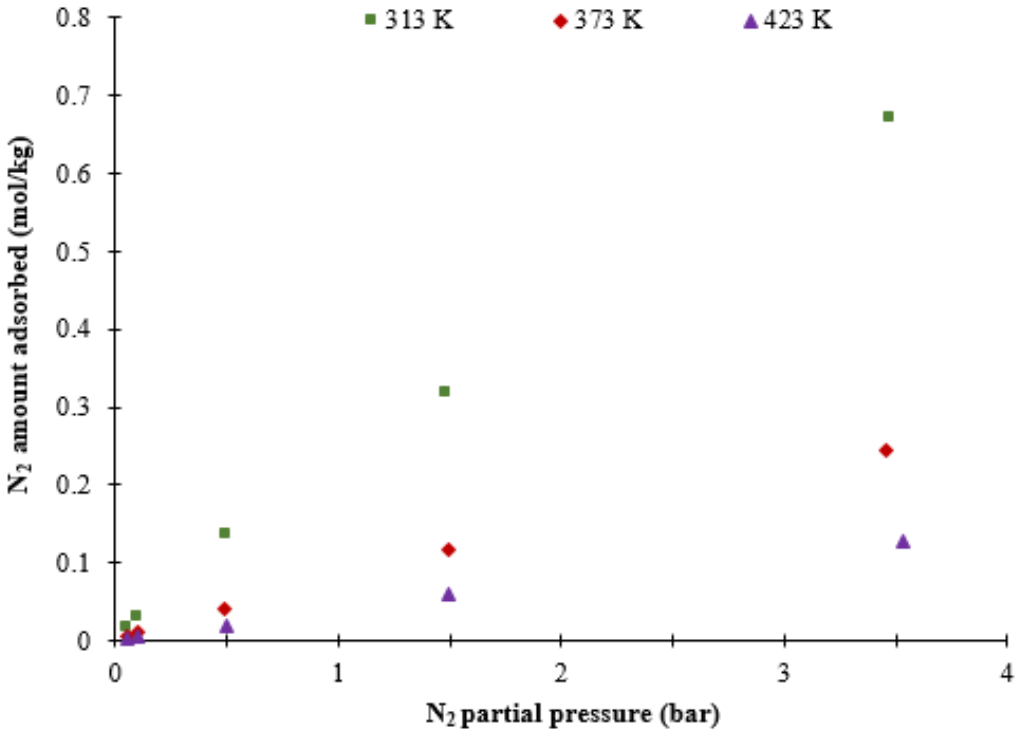

Figure 14: Adsorption Equilibrium Isotherms of N_2 on zeolites KY.

Table 7: Experimental conditions of all runs at 313, 373 and 423 K to study the N_2 adsorption on binder-free KY zeolite.

RUNS (313K)	**N_2 Flow (ml/min)**	**He Flow (ml/min)**	**Total Pressure (bar)**	**N_2 partial pressure (bar)**	**Loading (mol/kg)**
1.1	4.72	88.2	1	0.05	0.0158
1.2	9.20	83.4	1	0.1	0.0298
1.3	46.0	46.2	1	0.5	0.135
1.4	27.6	65.3	5	1.5	0.317
1.5	64.5	28.4	5	3.5	0.671
RUNS (373K)	**N_2 Flow (ml/min)**	**He Flow (ml/min)**	**Total Pressure (bar)**	**N_2 partial pressure (bar)**	**Loading (mol/kg)**
2.1	3.95	74.6	1	0.05	0.00568
2.2	7.80	69.4	1	0.1	0.00966
2.3	38.1	39.0	1	0.5	0.0402
2.4	23.1	54.1	5	1.5	0.116
2.5	53.7	23.9	5	3.5	0.246
RUNS (423K)	**N_2 Flow (ml/min)**	**He Flow (ml/min)**	**Total Pressure (bar)**	**N_2 partial pressure (bar)**	**Loading (mol/kg)**
3.1	3.42	65.1	1	0.05	0.00319
3.2	7.21	61.1	1	0.1	0.00551
3.3	34.3	34.1	1	0.5	0.0194
3.4	20.5	48.2	5	1.5	0.0597
3.5	48.4	20.1	5	3.5	0.128

As expected, the amount adsorbed of N_2 in zeolite KY increases by enhancing the partial pressure and decreases with increasing temperature at a fixed partial pressure, with a more linear behavior. The total amount adsorbed of N_2 is a lot less comparing it to CO_2, as the loading doesn't exceed 0.68 kJ/mol at the lowest temperature and highest partial pressure. This is more visible in Figure 18 where the adsorption capacity of both CO_2 and N_2 are compared at 313, 373 and 423 K.

Same as the procedure for CO_2, the isotherms were fitted by minimizing equation (15) and the Langmuir model was applied. Values of the Langmuir model parameters and coefficient of determination were determined, and listed in Table 8. The adsorption equilibrium isotherm of N_2 on binder-free KY zeolite by applying the Langmuir model is represented in Figure 15.

Table 8: Adsorption equilibrium Langmuir model parameters for N_2 on binder-free KY zeolite.

q_m (mol/kg)	b * (bar^{-1})	$-\Delta H$ (kJ/mol)	r^2 (-)
2.10	0.133	21.1	0.997

** The reference temperature used is 313.15 K*

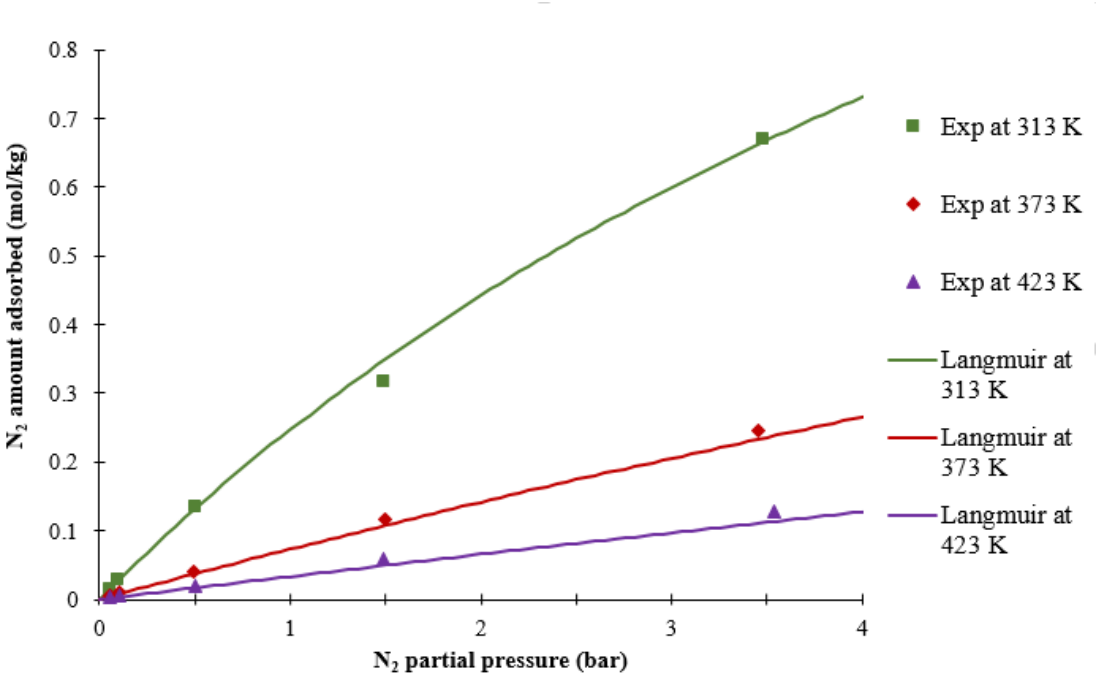

Figure 15: Adsorption equilibrium isotherms of N_2 on binder-free KY zeolite and fitting using the Langmuir model.

The heats of adsorption data were treated just as in the case of CO_2. Therefore, using equation (7), values of the isosteric heat is determined from the slope as shown in Figure 16.

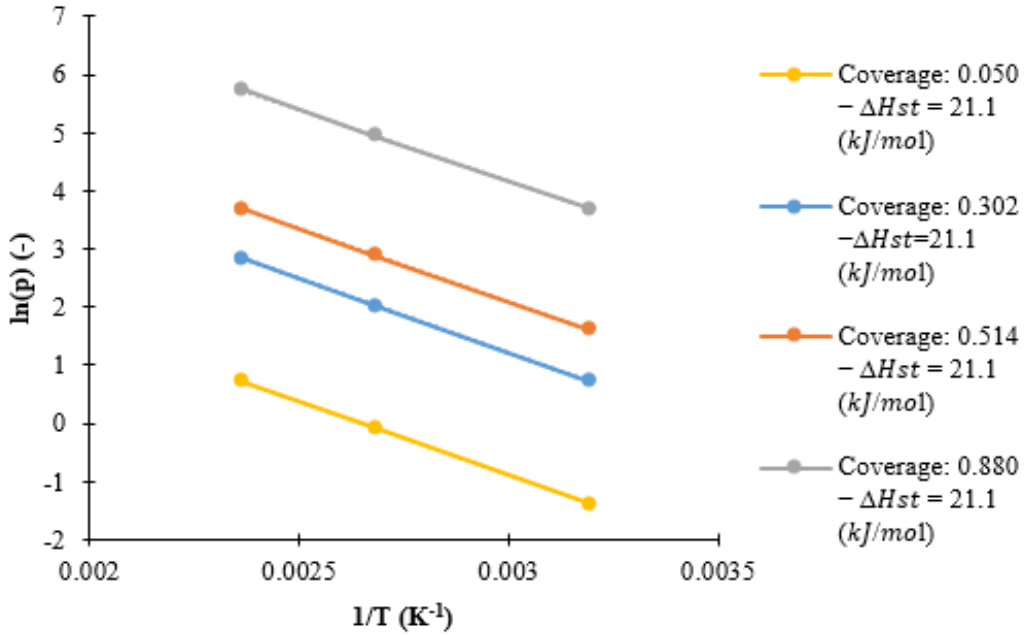

Figure 16: Plot of ln p over 1/T at fixed coverages for N_2 on binder-free KY.

As can be seen, the isosteric heat of sorption of N_2 on zeolites KY is constant. This means that the sites are homogeneous, and so the surface adsorption can be considered equal in all sites.

Indeed, even after applying the dual-site model Langmuir model and calculating the isosteric heat numerically, it is found that that the parameters in both sites are equal and that the value of the isosteric heat is constant over the capacity coverages: 21.1 $kJ.mol^{-1}$. This confirms the homogeneous behavior in the adsorption of N_2 in binder-free KY. Therefore, there is no need to use the DSL model as the Langmuir model is suitable enough, meaning that it is correct to assume that there is only one identical site instead of two different ones.

Figure 17 show a comparison between the N_2 isotherms collected in this work for binder-free KY and NaY at 298, 318 and 358 K, as shown in literature. [58] It is visible that the adsorption capacity of N_2 in binder-free KY is stronger than in NaY. This could mean that in the binary-component system, it is expected for the adsorption capacity of CO_2 to decrease due to the higher affinity of N_2 in binder-free KY.

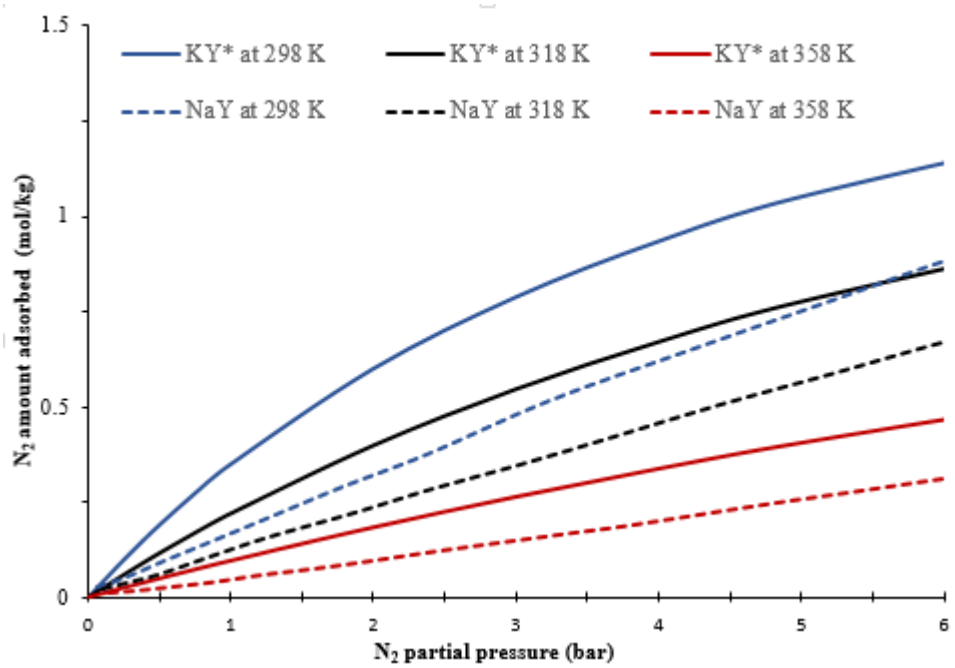

Figure 17: Comparison of N_2 adsorption isotherms in binder-free KY and NaY at different temperatures [58]. *The data for binder-free KY was measured in this work.

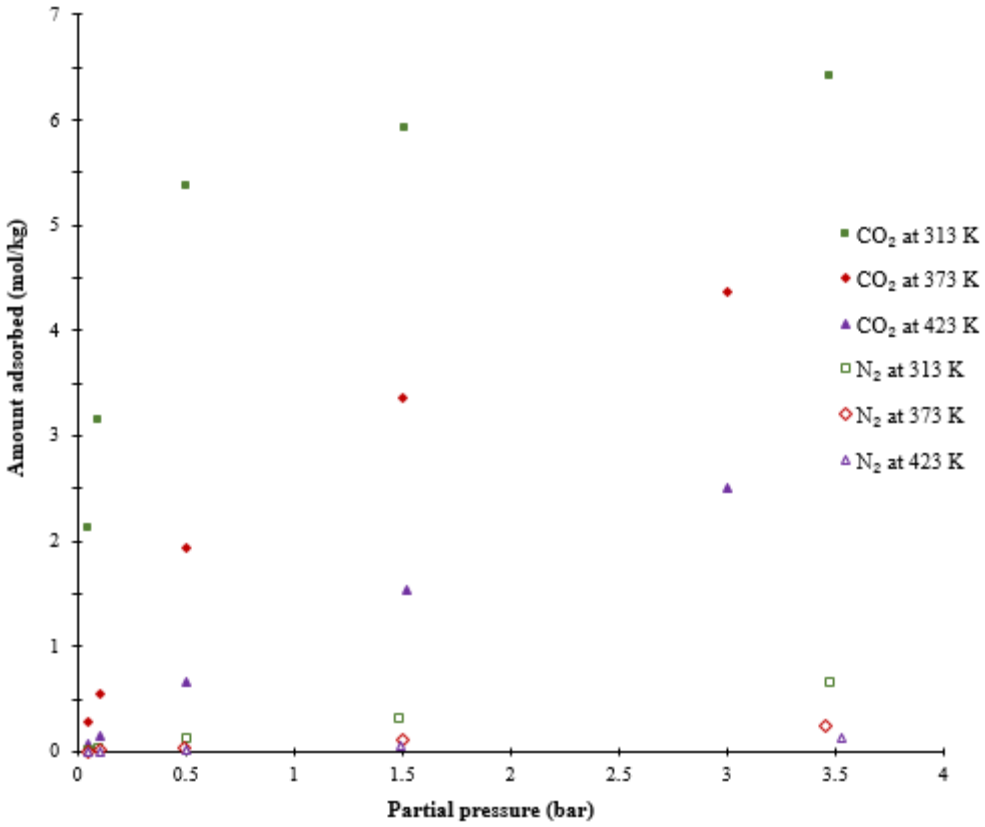

Figure 18: Adsorption Equilibrium Isotherms of CO_2 and N_2 on zeolites KY.

4.4. Binary-component adsorption of CO_2 / N_2 on binder-free KY

The actual flue gas from a coal-based power plant mainly consists of CO_2 and N_2 along with trace quantities of impurities like SOx, NOx, CO, moisture and other particulates. [55] The impurities present in the flue gas can have an influence on the adsorption capacities as these impurities will be competing with CO_2 for the sites available for adsorption. Also, the presence of certain impurities might also degrade the adsorbents over a period of time. Although these impurities will have an impact on the process performance, it is assumed the flue gas is composed of 15% CO_2 and 85% N_2. The assumption on the flue gas components would simplify the process and would allow us to provide key insights regarding the performances of zeolite KY on both carbon dioxide and nitrogen.

Figure 19 to 21 shows the adsorption breakthrough curves (a) and desorption breakthrough curves (b) for the mixture plotted as normalized molar fraction against time, where the effect of temperature on adsorption and desorption breakthrough curves are visible. The typical breakthrough time behavior was observed, as higher is the temperature lower is the breakthrough time. Unfortunately, the desorption step at 313 K (Figure 19 b) didn't reach to the end due to slow concentration decrease of CO_2 at 313 K. This is expected due to the high CO_2 affinity at low temperature.

Similar to the single-component system, the amount adsorbed of each temperature was determined directly from the breakthrough experiments, the resulting loading data are shown in Table 9. Furthermore, the extended DSL model for multicomponent systems (eq. 5) was used to predict the binary-component isotherms at 313 K, 373 K and 423 K, as shown in Figure 22.

Table 9: Binary-component experimental conditions of runs at 313 K, 373 K and 423 K.

Temperature (K)	**CO_2 Flow (ml/min)**	**N_2 Flow (ml/min)**	**Total Pressure (bar)**	**CO_2 partial pressure (bar)**	**CO_2 Loading (mol/kg)**
313	13.8	78.1	1	0.15	4.14
373	11.4	65.3	1	0.15	0.793
423	10.1	57.5	1	0.15	0.267

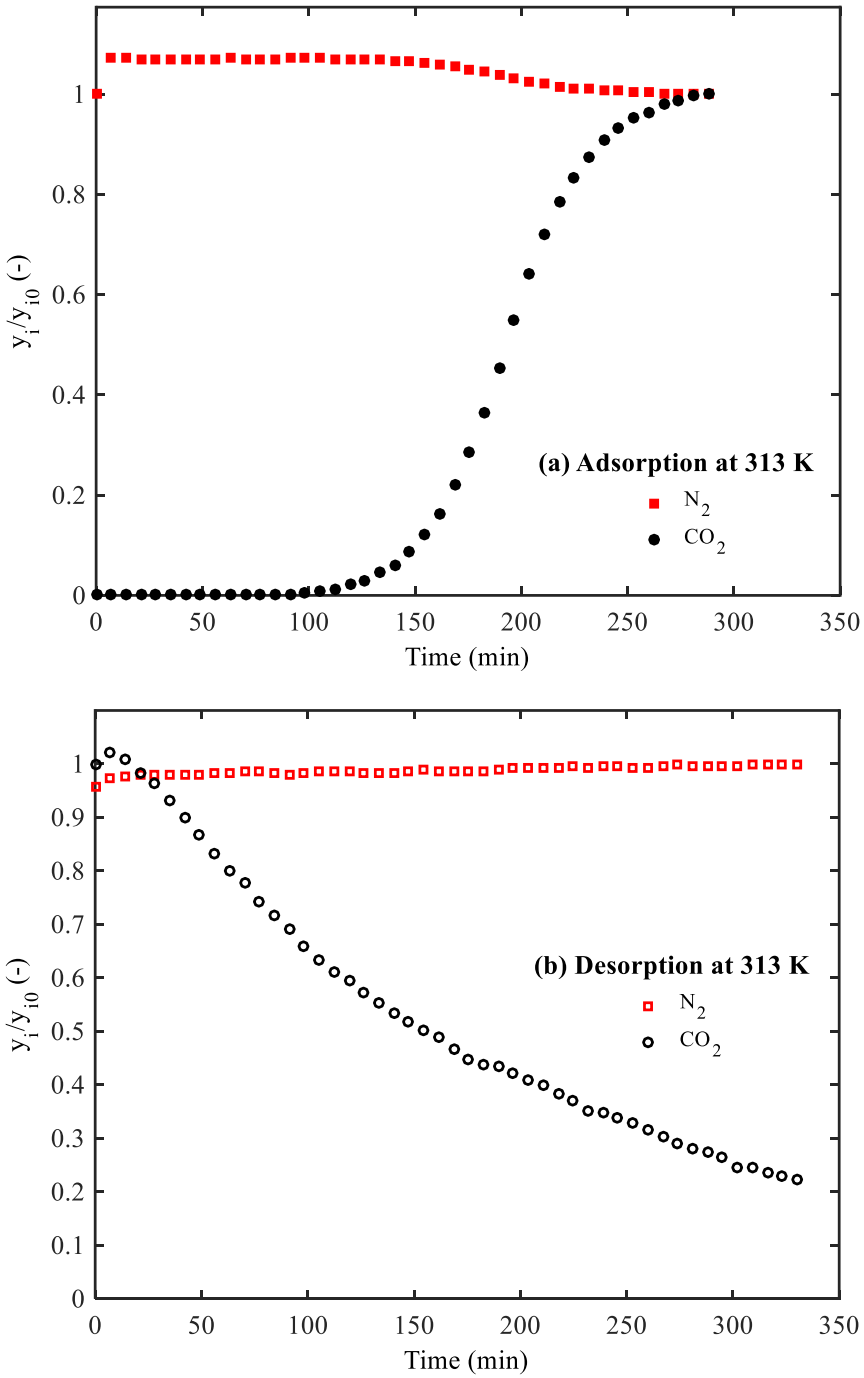

Figure 19: Adsorption (a) and desorption (b) breakthrough curves of binary mixtures CO_2 (15%) /N_2 (85%) on binder-free zeolite KY at 313 K.

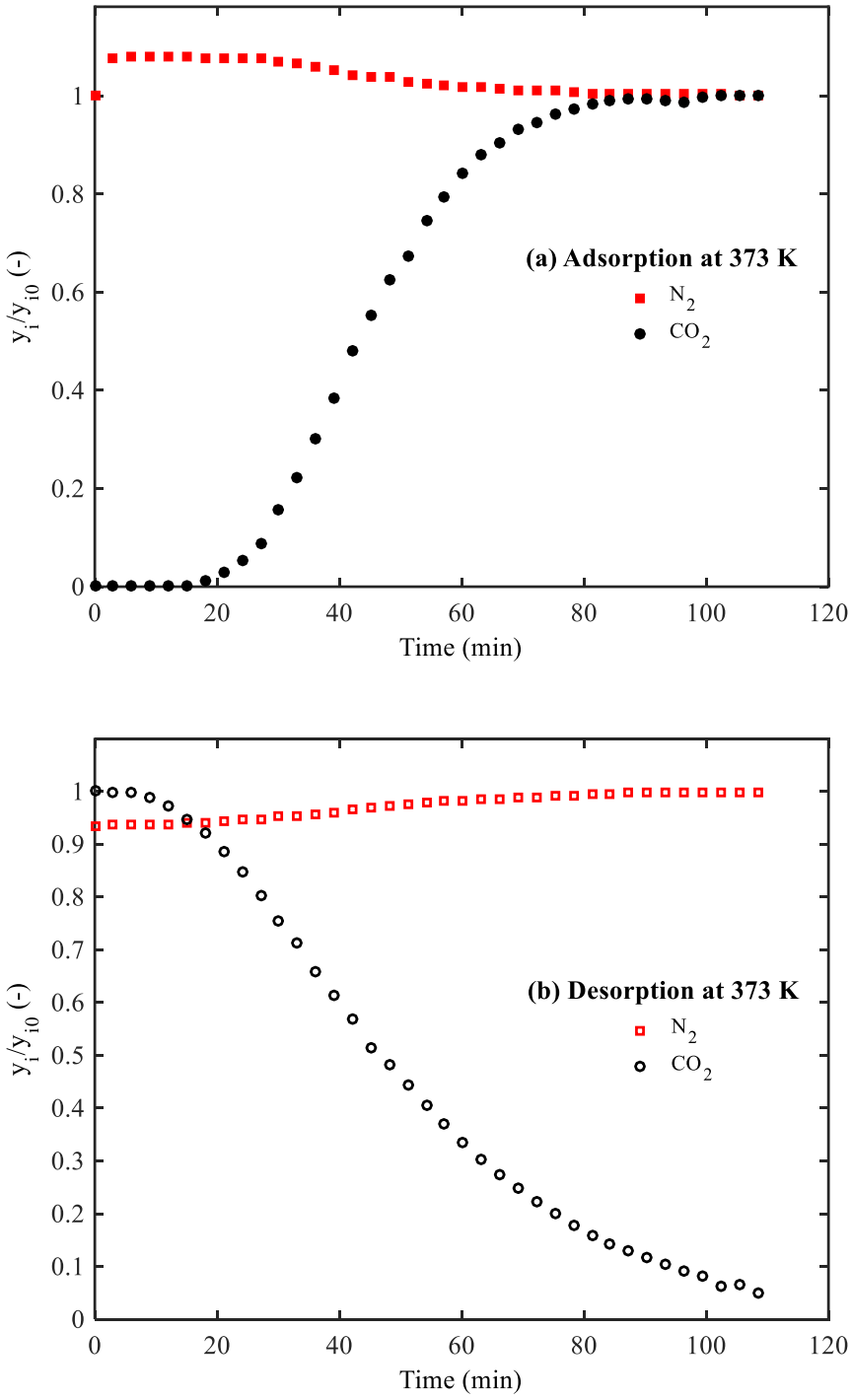

Figure 20: Adsorption (a) and desorption (b) breakthrough curves of binary mixtures CO_2 (15%) /N_2 (85%) on binder-free zeolite KY at 373 K.

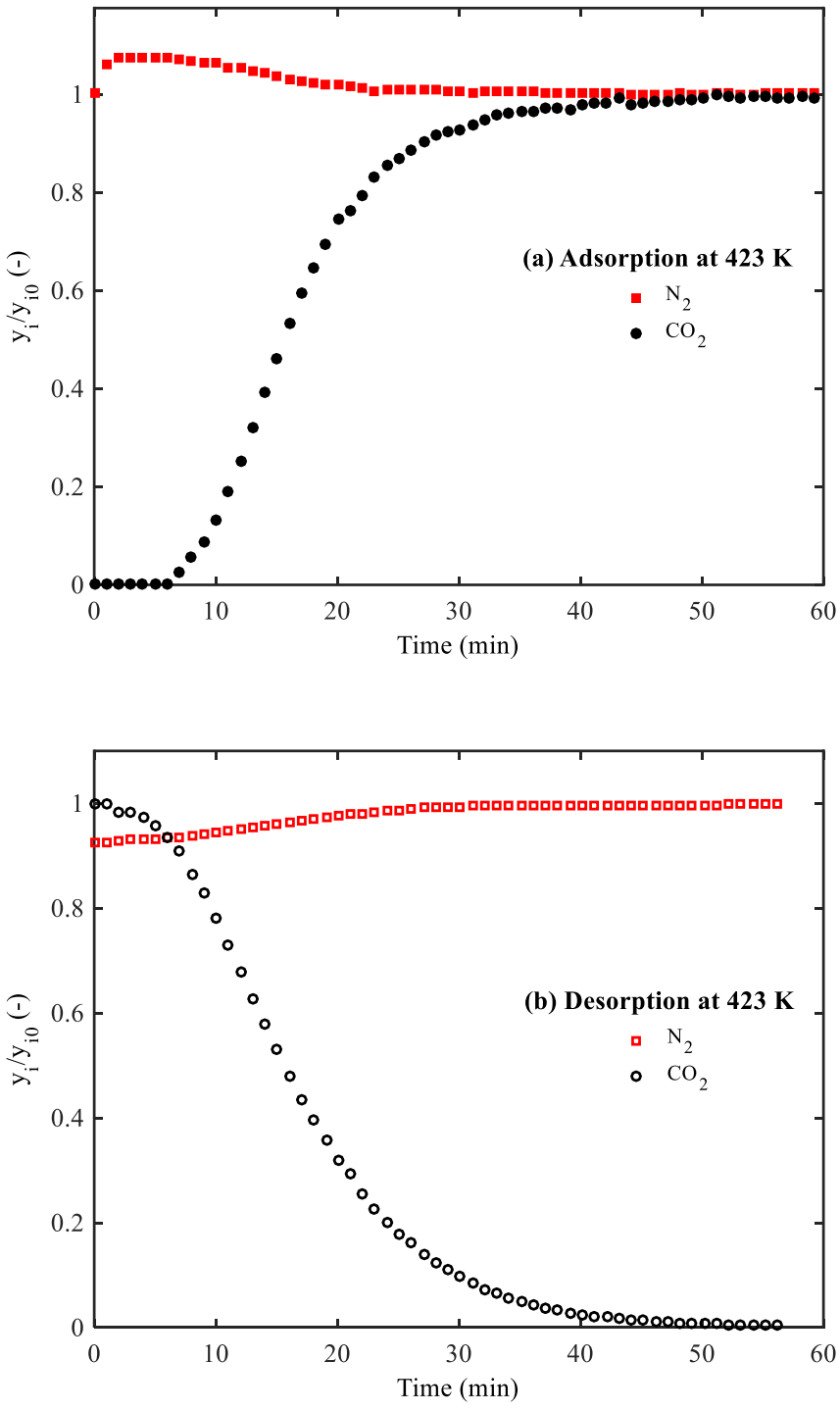

Figure 21: Adsorption (a) and desorption (b) breakthrough curves of binary mixtures CO_2 (15%) /N_2 (85%) on binder-free zeolite KY at 423 K.

Table 10: Adsorption equilibrium DSL model parameters for binary-component system of CO_2/ N_2 on binder-free KY zeolite.

	CO_2		N_2	
Site	*1*	*2*	*1*	*2*
q_m (mol/kg)	3.93	2.80	2.10	-
b (bar^{-1})	4.98	18.0	0.133	-
$-\Delta H$ (kJ/mol)	-38.3	-42.8	21.1	-
r^2 (-)		0.971		

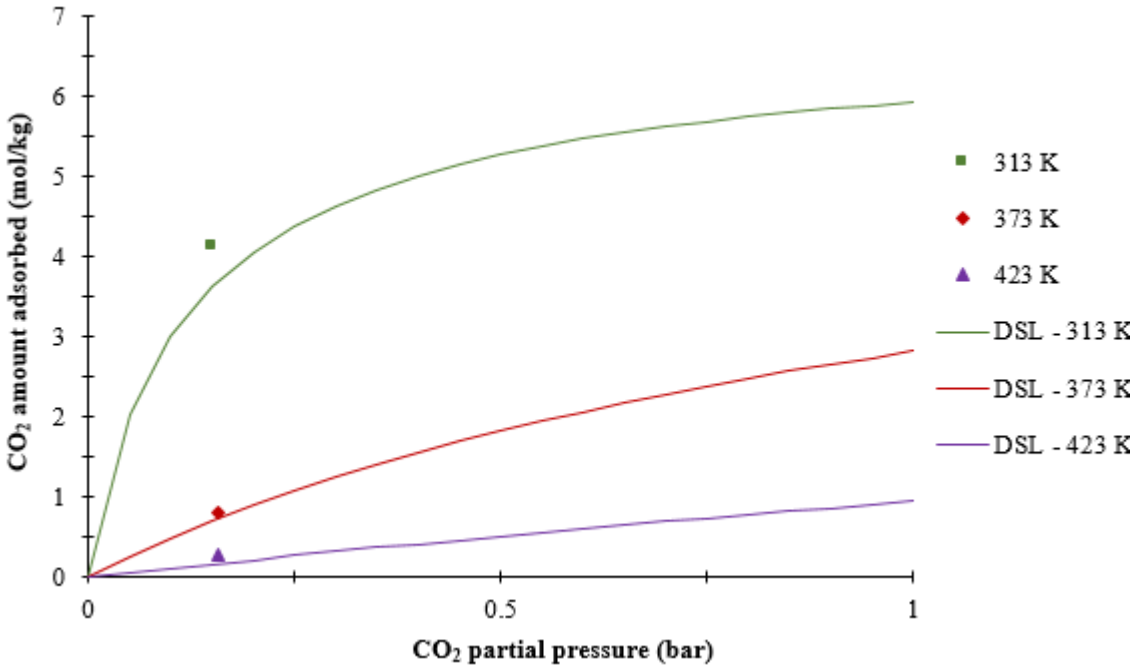

Figure 22: Adsorption equilibrium isotherms of binary-component system CO_2 / N2 on binder-free KY zeolite and fitting using the extended DSL model.

As be seen, the presence of N_2 in the stream slightly reduces the adsorption capacity of CO_2. Calculation of the adsorbent metrics can lead us to a more detailed evaluation.

4.5. Adsorbent Metrics on CO_2/ N_2 Isotherms

Using the extended DSL model isotherm to binary-component system (Figure 22), values of adsorption capacity, Henry selectivity, competitive selectivity, and competitive working capacity can be calculated (Eq. 10 - 14) at a typical post-combustion stream composed of 15% CO_2 and 85 % N_2 at 298 K. Table 11 shows the calculated values of binder-free KY metrics along with other adsorbents at flue gas conditions shown in literature [55]. Figure 23 shows a graphical representation of the selectivity of CO_2 over N_2, calculated using Equation 9. It is visible that at low pressure from 0 to 0.1 bar, the selectivity of CO_2 over N_2 is the highest as it goes over 105 at 313 K.

Table 11: Comparison of Adsorbent Metrics with different zeolites in CO_2 (15%) /N_2 (85%) stream.

Adsorbent metric	Adsorbents				
	Mg-MOF-74	Zeolite 13X	UTSA-16	CS-AC	Binder-free KY*
q_{CO2} $[mol/kg]$	<u>6.36</u>	3.44	2.33	0.900	4.66
Henry Selectvity (αH)	386	<u>834</u>	375	18.1	252
Pure Component Selectivity (α_P)	45.5	69.8	<u>201</u>	18.0	89.0
Competitive Component Selectivity (α_C)	404	<u>981</u>	375	60.6	251
Pure Working Capacity (β_C) [mol/kg]^{ad}	2.07	1.04	1.59	0.64	<u>4.67</u>
Competitive working Capacity (β_C) [mol/kg]^{ad}	2.05	1.03	1.58	0.51	<u>4.52</u>

**The data for binder-free KY was measured in this work.*
Conditions: [a]ads: q (T1, P1) = q (298 K, 1 bar). [d]des: q (T2, P2) = q (298 K, 0.03 bar).

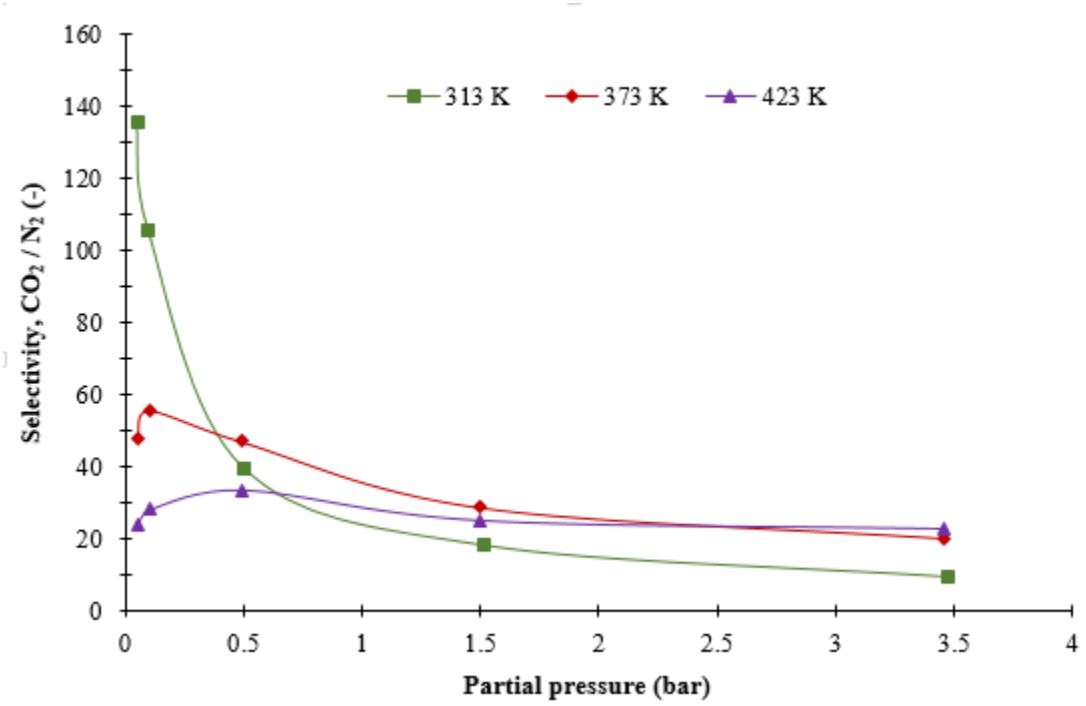

Figure 23: Selectivity of CO_2 / N_2 on binder-free KY at different temperatures.

As can be seen, comparing the adsorbent metrics values of binder-free KY to other adsorbents shown in Table 11, can give us an insight on the separation performance of CO_2 at flue gas conditions.

In terms of CO_2 loading, binder-free KY is 2nd best after Mg-MOF-74 which is understandable due to MOF's high surface area, large pore volume and strong interaction between CO_2 and the unsaturated metal sites. In terms of selectivities it is 2nd or 3rd best after zeolite 13X, along with Mg-MOF-74 and UTSA-16, this is due to the fact that zeolite 13X has smaller cation size (Na^+) and X zeolites are characterized with lower Si/Al ratio than Y zeolites therefore, there is a greater amount of exchangeable cations which are able to interact directly with the adsorbed CO_2 molecules. Furthermore, binder-free KY has the highest pure and competitive working capacity (0.03 bar – 1 bar) which indicates that the separation process of this adsorbent is better at low pressure.

4.6. Simulation of Binary Adsorption of CO_2/N_2 on binder-free zeolite KY

The modeling of breakthrough curves is the common way to gain insights about mass transfer mechanism as well as axial dispersion which impact the fixed bed adsorption processes. Thus, to help explaining the observations and to extend the range of predictions, an adsorption simulator available in our laboratory was used. [51, 63]

The adsorption simulator developed in MATLAB describes the adsorption dynamics in the column using a set of coupled non-linear partial differential equations model. The model is composed of total and component mass balance as well as energy balance equations which take into account the dispersive and convective effects to describe the heat transfer. Additionally, the mathematical model includes both the effect of axial dispersion and mass-transfer resistances considering the linear rate driving force model (LDF). [64]

Table 12: Mathematical Model Equations for Fixed Bed Adsorption simulator.

Phenomenon model	Equations	
ideal gas	$C = \frac{P}{RT}$	(17)
overall mass balance	$\frac{\partial F}{\partial z} + \varepsilon_b \frac{\partial C}{\partial t} + \rho_p(1-\varepsilon_b)\sum_{i=1}^{n}\frac{\partial \bar{q}_i}{\partial t} = 0$	(18)
component mass balance	$-\varepsilon_b D_{ax}\frac{\partial}{\partial z}\left(C\frac{\partial y_i}{\partial z}\right) + \frac{\partial (F y_i)}{\partial z} + \varepsilon_b \frac{\partial (C y_i)}{\partial t} + \rho_p(1-\varepsilon_b)\frac{\partial \bar{q}_i}{\partial t} = 0$	(19)
mass transfer rate	$\frac{\partial \bar{q}_i}{\partial t} = K_{LDF}(q^* - \bar{q}_i)$	(20)
Linear Driving Force (LDF)	$\frac{1}{K_{LDF}} = \frac{R_p}{3k_f} + \frac{R_p^2}{15\varepsilon_p D_p} + \frac{r_c^2}{15KD_c}$	(21)
gas-phase energy balance	$-K_{ax}\frac{\partial^2 T}{\partial z^2} + Fc_{pg}\frac{\partial T}{\partial z} + C\varepsilon_b C_{pg}\frac{\partial T}{\partial t} + (1-\varepsilon_b)a_p h_p(T-T_s) + a_c h_w(T-T_w) = 0$	(22)
solid-phase energy balance	$C_{ps}\frac{\partial T_s}{\partial t} = a_p h_p(T-T_s) + \rho_p \sum_{i=1}^{n}\left(-\Delta H_{st,i}\right)\frac{\partial \bar{q}_i}{\partial t}$	(23)
isotherm model (DSL)	$q_i = \frac{q_{m1} b_{1i} p_i}{1+\sum_{j=1}^{n} b_{1j} p_j} + \frac{q_{m2} b_{2i} p_i}{1+\sum_{j=1}^{n} b_{2j} p_j}$	(5)

The equations of adsorption simulator are summarized in Table 12. The assumptions of mathematical model are:

1. The gas is considered to follow the ideal gas law;
2. Constant bulk concentration in the bed;
3. The pressure drop is negligible;
4. The radial diffusion effects are negligible;
5. The adsorption equilibrium is described by Langmuir's isotherm;
6. The external resistance and macropore diffusion can be combined in a global resistance to a lumped model for the adsorbent particle (Linear Driving Force model – LDF).

The common approach used to describe the mass transfer kinetics in an adsorption column is the linear driving force (LDF) [64]. In this approach, the lumped parameter, the LDF coefficient or overall mass transfer coefficient, K_{LDF}, is related to the various resistances such as film diffusion, macropore, and micropore diffusion, given by the following equation,

$$\frac{1}{K_{LDF}} = \frac{R_p}{3k_f} + \frac{R_p^2}{15\varepsilon_p D_p} + \frac{r_c^2}{15KD_c} \qquad (21)$$

where K is the dimensionless Henry´s law equilibrium constant (-), R_p is the particle radius (m), ε_p is the particle porosity (-), D_p is the effective macropore diffusivty ($m^2 \cdot s^{-1}$), r_c is the crystal radius (m), and D_c is the intracrystalline diffusivity ($m^2 \cdot s^{-1}$).

Ruthven *et al.* [17] have proposed the method of moments for a linear system in order to evaluate the relative importance of the individual axial dispersion and mass-transfer resistances by an overall effective rate coefficient k′, given by following equation,

$$\frac{1}{k'K} = \frac{D_{ax}}{v_i^2}\left(\frac{1-\varepsilon_b}{\varepsilon_b}\right) + \frac{1}{K_{LDF}} \qquad (24)$$

where k' is the overall effective rate coefficient (s^{-1}), D_{ax} is the axial dispersion ($m^2 \cdot s^{-1}$), v_i is the interstitial velocity ($m \cdot s^{-1}$), ε_b is the bed porosity (-).

This method is an easy way to evaluate which is the dominant mass-transfer mechanism in the system by comparing the time of each parameter. Thus, to use this method we need to estimate the axial dispersion and overall mass transfer coefficient. There are in the literature correlations which provided good approximations to these parameters. Table 15, in Appendix D, summarizes and define some parameters that can be estimated from literature.

Table 13 summarizes each term of equations 21 and 24 for the binary experiments at 313, 373, and 423 K.

Table 13: Estimated parameters of axial dispersion and mass-transfer resistances from the method of moments for experimental breakthrough curves of CO_2/N_2 mixture.

T (K)	**Specie**	$\frac{D_{ax}}{v_i^2}\left(\frac{1-\varepsilon_b}{\varepsilon_b}\right)$ **(s)**	$\frac{Rp}{3k_f}$ **(s)**	$\frac{R_p^2}{15\varepsilon_p D_p}$ **(s)**	$\frac{r_c^2}{15KD_c}$ **(s)**	$\frac{1}{K_{LDF}}$ **(s)**
313	CO_2	1.81	0.01	0.04	2.11E-06	0.05
	N_2	1.81	0.01	0.04	1.24E-06	0.05
373	CO_2	2.33	0.01	0.03	4.98E-06	0.04
	N_2	2.33	0.01	0.03	7.73E-07	0.04
423	CO_2	2.77	0.01	0.02	6.76E-06	0.02
	N_2	2.77	0.01	0.01	5.67E-07	0.02

From Table 13 we can be seen that values of axial dispersion (1.81 to 2.77 s) are higher than the inverse of overall mass-transfer coefficient (0.05 to 0.02 s), which indicates that the axial dispersion has a significant influence on the shape of breakthrough curves.

To verify if the axial dispersion (D_{ax}) affects the spreading of breakthrough curves much than the overall mass transfer coefficient (K_{LDF}), we can perform a simulation by substitute the estimated parameters in the simulator. First, we can keep constant the axial dispersion and change the overall mass-transfer coefficient and then keep constant overall mass-transfer coefficient and change the axial dispersion to see the effects on the breakthrough curves. Here, the axial dispersion is shown in terms of Peclet number ($P_e = vL/D_{ax}$).

Figure 24 shows that with a little change of overall mass-transfer coefficient there is no effect in the breakthrough curves. On the other hand, Figure 25 shows different spreading of breakthrough curves as a function of the Peclet number. This parametric study clearly shows that zone spreading in the bed is completely dominated by axial dispersion and confirm the prediction of method of moments.

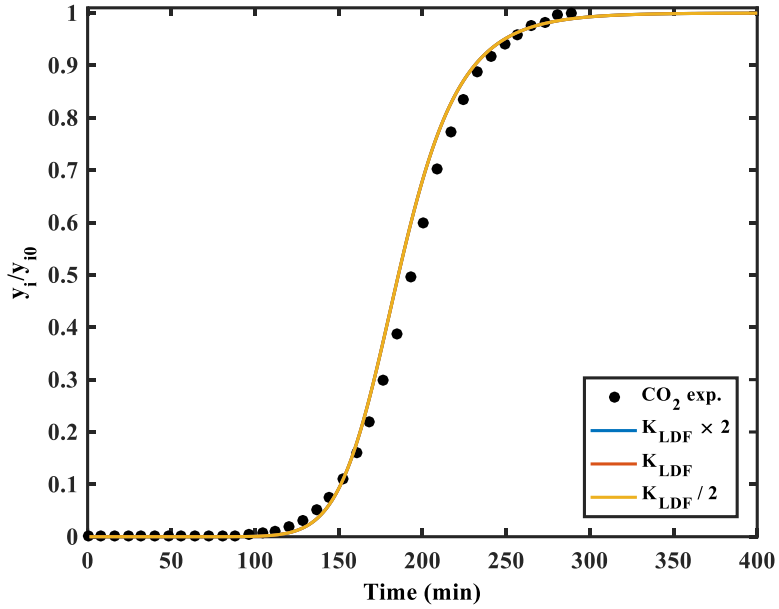

Figure 24: Influence of overall mass transfer coefficient on numerical breakthrough curve of CO_2 at 313 K and 0.15 bar partial pressure balanced with N_2

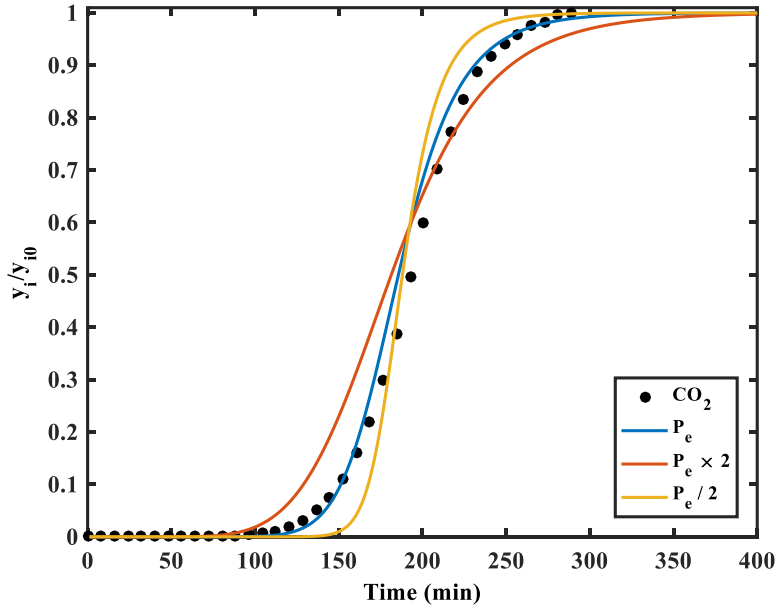

Figure 25: Influence of Peclet number on numerical breakthrough curve of CO_2 at 313 K and 0.15 bar partial pressure balanced with N_2.

After performing the parametric study and gain insights about the mass transfer mechanism, we can carry out the simulation knowing that the breakthrough curve spreading is affected by axial dispersion. Table 14 summarizes the calculated parameters for the simulation of binary experiment. The correlation used to estimate the model parameters as well as the assumption are in Table 15 in Appendix D.

Table 14: Calculated model parameters for the simulation of binary adsorption (Ads) and desorption (Des) breakthrough experiments.

T (K)	Step	K_{LDF} (s^{-1})		D_{ax} (m^2/s)	K_{ax} (W/m/K)	C_{pg} (J/mol/K)	h_p (W/m/K)	h_w (W/m/K)
		CO_2	N_2					
313	Ads	18.6	19.6	5.10×10^{-05}	0.16	30.4	36.3	30.0
	Des	18.6	19.6	2.92×10^{-05}	0.16	30.4	35.7	30.0
373	Ads	24.6	26.3	4.26×10^{-05}	0.16	30.8	40.6	30.0
	Des	24.6	26.3	4.91×10^{-05}	0.16	30.8	40.1	30.0
423	Ads	44.0	47.0	6.33×10^{-05}	0.16	31.2	44.1	30.0
	Des	43.9	46.9	4.42×10^{-05}	0.16	31.2	43.6	30.0

Figures 26, 27 and 28 show the simulation (lines) and experimental (symbols) breakthrough curves for adsorption and desorption of CO_2 on binder-free zeolite KY at 313, 373, and 423 K, respectively. As can be seen, the simulation result was in a good agreement of experimental data.

As mentioned above, for the desorption step at 313 K (Figure 26) the CO_2 concentration did not reach to the end due to slow decrease. However, from the simulator we can have an idea how long the CO_2 stay inside the column and hence compare to the other conditions. Figure 26 shows that the CO_2 stay inside the column at least 1000 min, being a very long time compared to desorption time at 423 K (Figure 28). As temperature increased (Figure 26 to 28), CO_2 was desorbed more rapidly from the column and the CO_2 concentration correspondingly decreases more rapidly. This observation agree with the selectivity shows in Figure 23.

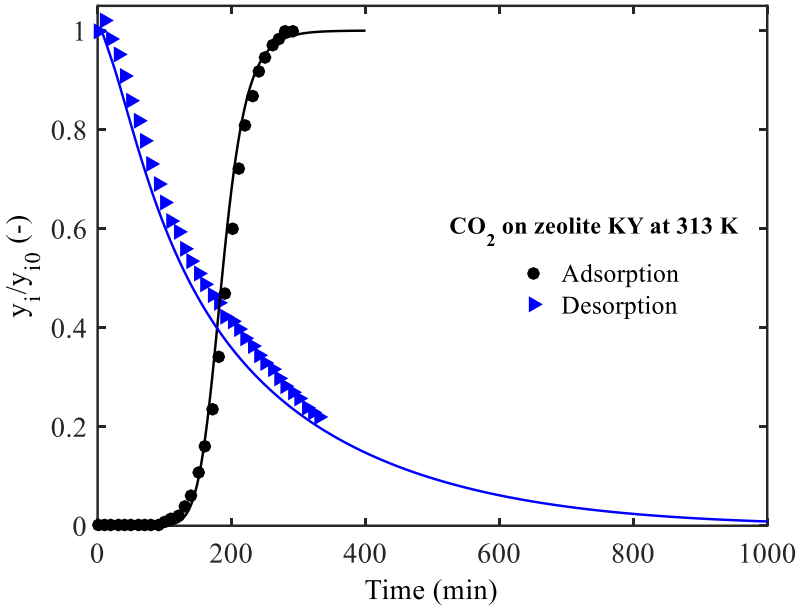

Figure 26: Adsorption and desorption breakthrough curves for CO_2 on binder-free zeolite KY at 313 K. The column is first saturated with N_2 (1 bar), and then, it is fed a gas mixture (15% CO_2 balanced with N_2). Experimental = symbols; Lines = simulations.

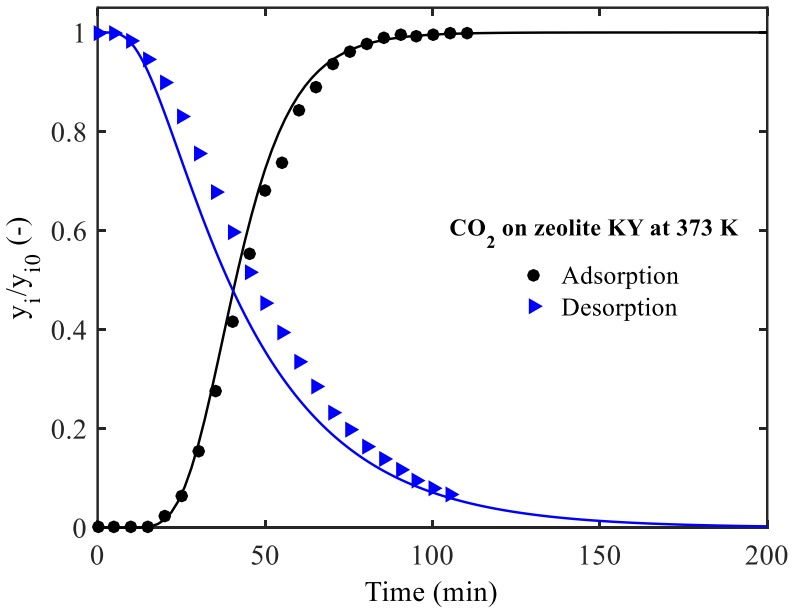

Figure 27: Adsorption and desorption breakthrough curves for CO_2 on binder-free zeolite KY at 373 K. The column is first saturated with N_2 (1 bar), and then, it is fed a gas mixture (15% CO_2 balanced with N_2). Experimental = symbols; Lines = simulations.

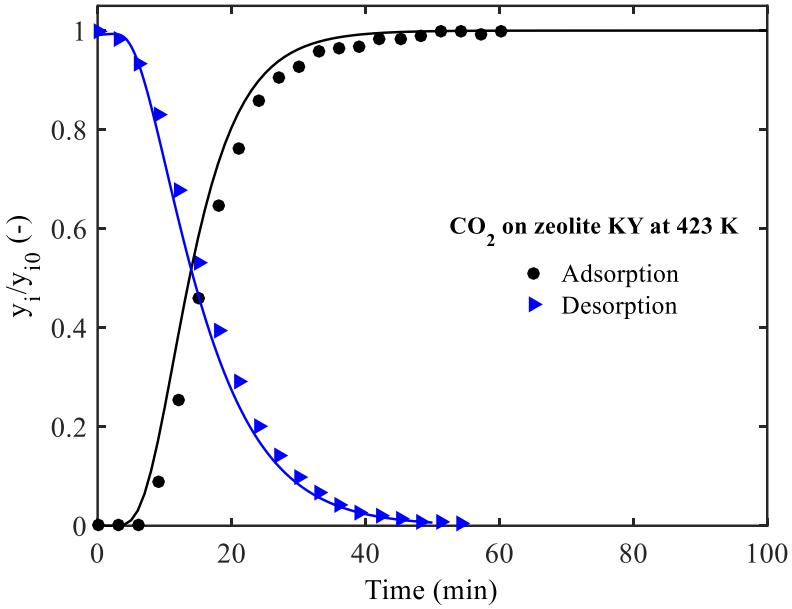

Figure 28: Adsorption and desorption breakthrough curves for CO_2 on binder-free zeolite KY at 423 K. The column is first saturated with N_2 (1 bar), and then, it is fed a gas mixture (15% CO_2 balanced with N_2). Experimental = symbols; Lines = simulations.

The adsorption of CO_2 on binder-free zeolite KY is highly impacted to temperature which is a great characteristic of Temperature Swing Adsorption processes. From the amount adsorbed of CO_2 at binary conditions (see Table 9) it is possible to predict the working capacity between two different temperature keeping the same feed condition. For instance, for a feed gas mixture of 15% CO_2 and 85 % N_2, and adsorption conditions of 313 K and 1 bar (representing the low temperature), and desorption conditions of 423 K and 1 bar (representing the high temperature), the working capacity is 3.87 mol/kg. To the same conditions, the working capacity of 13X is equal to 2.64 mol/kg, being lower than binder-free zeolite KY studied in this work. The working capacity of 13X was calculated using the pure equilibrium parameters reported in [55]. This result agrees with the observation that the CO_2 is more adsorbed on binder-free zeolite KY than zeolite 13X at low pressures. The post-combustion streams are released off at atmospheric pressure and a low fraction of CO_2. Thus, a material that has a great working capacity at low pressures is desired to recover CO_2 from post-combustion streams, and it makes the binder-free zeolite KY one interesting material for this application.

Another parameter that affects the CO_2 desorption is the N_2 purge rate. The N_2 purge rates used in the desorption experiment performed in this work are constant and equal to the initial value of the adsorption experiment (see Table 7). However, from the simulator, we are able to predict how the CO_2 profiles in the desorption step will behave as an increase of N_2 purge rates. Figure 29 shows the profiles of CO_2 normalized concentrations during desorption with various N_2 purge rates for the binary experiment at 373 K. As can be seen, as higher as N_2 purge rate more quickly CO_2 is desorbed from the column. To compare the N_2 purge time at different N_2 purge rates, we define the target of N_2 purge time when the CO_2 normalized concentration reaches 5 %, represented by the dashed line in Figure 29. Also, the arrows indicated the N_2 purge time for each N_2 purge rate. As well known that the main cost in an adsorption application comes from the desorption step which spent energy on heating and purges gas to clean and desorbs target species [55, 65-69]. Thus, a decrease in these parameters is always desired. Regarding Figure 29, comparing the profiles using 82 mL/min with 246 mL/min, it is possible to reduce the total volume of N_2 purge used in the desorption step by at least 13 % and reduce the N_2 purge time up to 71 %.

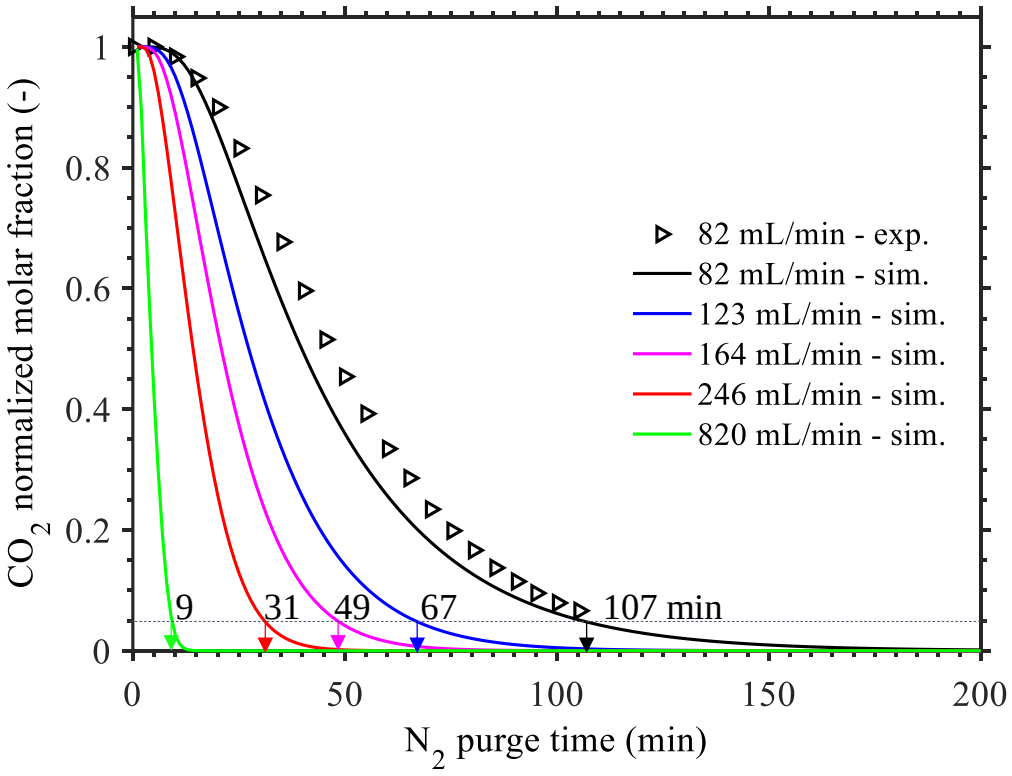

Figure 29: Profiles of CO_2 normalized concentrations during desorption with various N_2 purge rates at a fixed temperature of 373 K.

5. CONCLUSION

Adsorption equilibrium data were measured for CO_2 and N_2 on commercial binder-free KY zeolite from a breakthrough chromatographic technique. The data collected was compared with other Y zeolites modified by alkali metal cation exchanged from literature. In general, the experimental results show that the largest CO_2 capacities were obtained by the binder-free KY in the low-pressure region. At 373 K and 1.5 bar, the CO_2 loading on binder-free KY is equal to 3.36 mol/kg compared to 2.52 mol/kg for NaY; 1.85 mol/kg for LiY; 2.15 mol/kg for CsY. This is due to (a) the response of the acidic CO_2 to the basic properties of the zeolites containing large molecules; (b) the large cavities in faujastie-type zeolites that makes it easy for K^+ ions to become preferential adsorption center for CO_2, and (c) high values of heats of adsorption indicating strong interactions between the adsorbed molecules and K+ ions. In addition, the commercial binder-free type KY was responsible for the improvement of up to 20 % for the CO_2 loading compared to the standard binder KY under the same conditions. In terms of N_2 loading, values were much lower compared to CO_2, as the maximum experimental loading 0.671 mol/kg was reached at the lowest temperature and highest partial pressure (313 K, 3.5 bar).

Furthermore, the binary-component experiments were carried out in a typical post-combustion flue gas stream consisting of 15% of CO_2 and 85% N_2, and the separation performance of CO_2 from the stream was evaluated using adsorbent screening metrics. At 298 K, the CO_2 amount adsorbed of the binder-free KY is 4.66 mol/kg compared to 6.36 mol/kg and 3.44 mol/kg for Mg-MOF-74 and zeolite 13X, respectively. Between 0.03 bar and 1 bar, the average working capacity of binder-free KY is the highest with 4.59 mol/kg compared to only 2.06 mol/kg for Mg-MOF-74 and 1.03 mol/kg for and zeolite 13X. At 313 K and 0.1 bar, the selectivity of CO_2 over N_2 is high, with the value to 105. The results indicate that the CO_2 separation performance of binder-free KY is ideal at low pressure, which is a great feature for the capture of CO_2 from post-combustion streams.

Simulation results were also performed using a numerical technique developed in MATLAB to study the mass-transfer mechanics of CO_2 and N_2 onto binder-free zeolite KY. The parametric study clearly showed that zone spreading in the bed is completely dominated by axial dispersion. Additionally, from the simulator it was possible to study the effect of N_2 purge flow

rate, and it was shown that it is possible to reduce the total volume of N_2 purge used in the desorption step by at least 13 % while reducing the N_2 purge time up to 71 %.

Future Work:

The results discussed in this work show that the binder-free zeolite KY is a promising adsorbent as it has great characteristics to be applied at CO_2 recovery from the post-combustion streams. However, all efforts of this work were focused on fixed bed experiments which allow us to better-know the interaction between adsorbent material and adsorbable species, but it does not allow us to visualize the performance of CO_2 recovery in cyclic adsorption processes. Therefore, for future work, it is highly suggested to study the binder-free zeolite KY for CO_2 recovery by cyclic Pressure Swing/ Temperature Swing Adsorption processes.

REFERENCE

[1] P. Li and F. H. Tezel, "Pure and Binary Adsorption Equilibria of Carbon Dioxide and Nitrogen on Silicalite." *American Chemical Society*, vol. 53, no. 11, pp. 2479–2487, 2008.

[2] Y. Zou and A. E. Rodrigues, "Adsorbent Materials for Carbon Dioxide" *Adsorption Science & Technology*, vol. 19, no. 3, pp. 255-266, 2001.

[3] E. T. Sundquist and K. Visser, "The geologic history of the carbon cycle" *Treatise on Geochemistry*, vol. 10, pp. 425–472, 2014.

[4] H. B. Dulal and S. Akbar, "Greenhouse gas emission reduction options for cities: finding the ''Coincidence of Agendas'' between local priorities and climate change mitigation objectives." *Habitat Int*, vol. 38, pp.100-105, 2013.

[5] M. A. Kinnon and S. Samuelson, "The role of natural gas and its infrastructure in mitigating greenhouse gas emissions, improving regional air quality, and renewable resource integration", *Progress in Energy and Combustion Science.*, vol. 64, pp. 62-92, 2018.

[6] H. Ritchie (2017) "Fossil Fuels". *OurWorldInData.org*. Available: https://ourworldindata.org/fossil-fuels Last accessed 9th Oct 2020.

[7] M. Younas, M. Sohail, L. K. Leong, M. J. K Bashir, S. Sumanthi "Feasibility of CO_2 adsorption by solid adsorbents: a review on low-temperature systems", *Int. J. Environ. Sci Technol.*, vol. 13, pp. 1839-1860, 2016.

[8] T. L. P. Dantas, A. E. Rodrigues, R. F. P. M. Moreira "Separation of Carbon Dioxide from Flue Gas Using Adsorption on Porous Solids", *InTech*, pp. 57 – 80, 2012.

[9] K. Thambimuthu, M. Soltanieh, J. C. Abanades, *Carbon dioxide Capture and Storage*. Cambridge: Cambridge University Press. p.109, 2005.

[10] M. Kanniche *et al.* "Pre-combustion, Post-combustion and Oxy-combustion in thermal power plant for CO capture." *Applied Thermal Engineering, Elsevier*, vol.30, no. 1, p.53, 2009.

[11] R. l. Meacham, "SORPTION-EFFECT CHROMATOGRAPHY"**,** *A Doctoral Thesis*, Loughborough University of Technology, 1990.

[12] H. Yang, Z. Xu, M. Fan , R. Gupta, R.B. Slimane, A.E Bland, I. Wright, "Progress in carbon dioxide separation and capture." *J Environ Sci*, vol. 20, no. 1, pp. 14-27, 2008.

[13] Q. Wang, J. Luo, Z. Zhong, A. Borgna, "CO_2 capture by solid adsorbents and their applications: current status and new trends." *Energ. Environ. Sci.* vol.4, no. 1, pp. 42–55, 2011.

[14] D. Bonenfant, M. Kharoune, P. Niquette, M. Mimeault, R. Hausler, "Advances in principal factors influencing carbon dioxide adsorption on zeolites." *Sci. Technol. Adv. Mater.,* vol. 9, pp. 7–13, 2008.

[15] S. Montalvo, L. Guerrero and R. Borja, "Application of natural zeolites in anaerobic digestion processes" *Applied Clay Science,* vol. 58, no.1, pp.125-133, 2012.

[16] R. Triebe. "Seperation and Purification of Gases with Molecular Sieves." *A Master Dissertation*, University of Ottawa, 1994.

[17] D. M. Ruthven, *Principles of Adsorption and Adsorption Processes*, 1st ed. New York: John Wiley & Sons, 1984.

[18] D. W. Breck, *Zeolite Molecular Sieves*, 1st ed. New York: John Wiley & Sons, 1974.

[19] Chemical book. (2017) "Zeolite".
Available: https://www.chemicalbook.com/ProductCatalog_EN/2220.htm Last accessed 9th Oct 2020.

[20] K. S. Walton, M. B. Abney, M. D. LeVan. "CO_2 adsorption in Y and X zeolites modified by alkali metal cation exchange." *Microporous and Mesoporous Materials*, vol. 91, pp. 78-84, 2006.

[21] L.B. McCusker, C. Baerlocher, "Zeolite structures." *Studies in surface science and catalysis*, vol. 137, pp. 37–67, 2001

[22] J.R. Smyth and F.A. Caporuscio, "Review of the Thermal Stability and Cation Exchange Properties of the Zeolite Minerals Clinoptilolite, Mordenite, and Analcime: Applications to Radioactive Waste Isolation in Silicic Tuff" *Master Dissertation,* University of California, 1981.

[23] J. A. C. Silva, K. Schumann, A. E. Rodrigues. "Sorption and kinetics of CO_2 and CH_4 in binder-free beads of 13X zeolite." *Microporous and Mesoporous Materials,* vol. 158, pp. 219-228, 2012.

[24] J. A. C. Silva. *et al.* "Adsorption Equilibrium and Dynamics of Fixed Bed Adsorption of CH_4/N_2 in Binder-free Beads of 5A Zeolite." *Ind. Eng. Chem. Res.*, vol.54, pp. 6390−6399, 2015.

[25] J. A. C. Silva, A.F. Cunha, K. Schumann, A. E. Rodrigues, "Binary Adsorption of CO_2/CH_4 in Binder-free Beads of 13X Zeolite." *Microporous Mesoporous Mate*r., vol. 187, pp. 100-107, 2014.

[26] K. Schumann, B. Unger, A. Brandt, F. Scheffler, "Investigation on the pore structure of binderless zeolite 13× shapes" *Microporous Mesoporous Mater*, vol. 154, pp.119-123, 2012.

[27] S. O. Yong, D. C. W. Tsang, J.M. Novak, *Biochar from Biomass and Waste*. 1st ed. Chennai, India: Candince Janco, pp.169 – 209, 2019.

[28] V. Goetz, O. Pupier, A. Guillot, "Carbon dioxide-methane mixture adsorption on activated carbon." *Adsorption*, vol.12, no. 1, pp. 55–63, 2006.

[29] T.H. Ho, T. Howes, B.R. Bhandari, "Encapsulation of gases in powder solid matrices and their applications." *Powder Technol*, vol. 259, pp. 87–108, 2014.

[30] D.M. Ruthven, *Encyclopedia of Separation Technology*, 1st ed. New York: John Wiley & Sons, 1997.

[31] Y. Zou and A. E. Rodrigues "Adsorbent Materials for Carbon Dioxide", *Adsorption Science & Technology*, vol. 19, no. 3, pp. 255-266, 2001.

[32] A Khelifa, Z. Derriche, A. Bengueddach. "Sorption of carbon dioxide by zeolite X exchanged with Zn^{2+} and Cu^{2+}". *Microporous and Mesoporous Materials*, vol. 32, no. 1, pp. 199-209, 1999.

[33] T. D. Pham, R. Xiong, S.I. Sandler, R.F. Lobo, "Experimental and computational studies on the adsorption of CO_2 and N_2 on pure silica zeolites". *Micropor Mesopor Mat*, vol. 185, pp. 157–166, 2014.

[34] M.R. Hudson, W. L. Queen, J. A. Mason, D. W. Fickel, R. F. Lobo, C. M. Brown, "Unconventional, highly selective CO_2 adsorption in zeolite SSZ-13*". J Am Chem Soc*, vol. 134, pp. 1970–1973, 2012.

[35] Z. H. Y. Wang, B. B. Shah, D. Zhao, "CO_2 Capture in Metal–Organic Framework Adsorbents: An Engineering Perspective." *Advances Sustainable Systems*, vol. 3, no. 1, 2019.

[36] D. Farrusseng, *Metal-Organic Frameworks: Applications from Catalysis to Gas Storage*. Germany: Wiley-VCH. pp. 99-121, 2011.

[37] Y. Belmabkhout, M. Frère and G. D. Weireld, "High-pressure adsorption measurements. A comparative study of the volumetric and gravimetric methods." *Measurement Science and Technology*, vol. 15, no. 5, 2004.

[38] B. V. Kuznetsov, A. A. Moreva, T. A. Rakhmanova, "A comparison of the gravimetric, volumetric, and gas-chromatographic methods for measuring adsorption values." *Russian Journal of Physical Chemistry*, vol.74, pp. 1664-1669, 2000.

[39] G. Narin, S. Yilmaz, S. Ulku "A Chromatographic Study of Carbon Monoxide Adsorption in Clinoptilolite", *A Master Dissertation*, Izmir Institute of Technology, 2001.

[40] H. Marsh, F. Rodríguez-Reinoso. *Activated Carbon.* UK: Elsevier. pp. 143-242, 2006.

[41] G. D. Pirngruber, P. Raybaud and Y. Belmabkhout, "The role of the extra-framework cations in the adsorption of CO_2 on faujasite Y." *Physical Chemistry Chemical Physics*, vol.12, no. 41, pp. 13345- 13852, 2010.

[42] D. Verboekend, N. Nuttens, R. Locus, J. Van Aelst, "Synthesis, characterisation, and catalytic evaluation of hierarchical faujasite zeolites: milestones, challenges, and future directions." *Chemical Society Reviews*, vol. 42, no.1, pp. 3331-3352, 2016.

[43] S. S. Khvoshchev and A. V. Zverev. "Calorimetric Study of NH3 and CO_2 Adsorption on Synthetic Faujasites with Ca^{2+}, Mg^{2+}, and La^{3+} Cations". *L V. Grebenshchikov Institute of Silicate Chemistry*, vol.144, no.2, pp.571-579, 1991.

[44] R. M. Barrer, *Zeolites and Clay Minerals as Sorbents and Molecular Sieves*, 1st ed. London: Academic Press, 1978.

[45] A Khelifa, Z. Derriche, A. Bengueddach. "Sorption of carbon dioxide by zeolite X exchanged with Zn^{2+} and Cu^{2+}". *Microporous and Mesoporous Materials*, vol. 32, no. 1, pp. 199-209, 1999.

[46] A. Khelifa, L. Benchehida, Z. Derriche, "Adsorption of carbon dioxide by X zeolites exchanged with Ni^{2+} and Cr^{3+}: isotherms and isosteric heat." *Journal of Colloid and Interface Science*, vol. 278, no. 1, pp. 9-17, 2004.

[47] T. M. Amelitcheva, L. L. Bogomolova, A. V. Kiselev, "Adsorption of ethane and ethylene by zeolites MgNaX and CaNaX with different degrees of ion exchange." *Journal of the Chemical Society*, vol.74, pp. 306-315, 1978.

[48] D. D. Do. *Adsorption Analysis: Equilibria and Kinetics*. Volume 2. London: Imperial College Press, 1998.

[49] N. A. Rashidi, S. Yusup, A. Borhan, "Isotherm and thermodynamic analysis of carbon dioxide on activated carbon." *Procedia Eng*, vol.148, pp. 630–637, 2016.

[50] B. H. Hameed and K. Y. Foo, "Insights into the modeling of adsorption isotherm systems," *Elsevier*, vol. 8, pp. 2–10, 2010.

[51] L. F. A. S. Zafanelli, A. Henrique, M, Karimi, A. E. Rodrigues, J. A. C. Silva, "Single- and Multicomponent Fixed Bed Adsorption of CO_2, CH_4, and N_2 in Binder-Free Beads of 4A Zeolite" *Industrial & Engineering Chemistry Research*, vol. 59, no.30, pp. 13724-13734, 2020.

[52] P. J. Harlick, F. H. Tezel, "An experimental adsorbent screening study for CO_2 removal from N_2." *Microporous Mesoporous Mater.* vol.76, no.13, pp. 71-79, 2004.

[53] R. Yang, *Gas Separation by Adsorption Processes*. London: .Imperial College Press, 1997.

[54] K. S. Knaebel, "For your next separation consider adsorption." *Chem. Eng*, vol.102, no. 11, 1995.

[55] A. K. Rajagopalan, A.M. Avila, A. Rajendran, "Do adsorbent screening metrics predict process performance? A process optimisation based study for post-combustion capture of CO_2." *Int. J. Greenh. Gas Control.*, vol. 46, pp. 76-85, 2016.

[56] X. Fang, P. Xiap, P. A. Webley. "CO_2 capture using a novel hybrid monolith (H-ZSM5/activated carbon) as adsorbent by combined vacuum and electric swing adsorption (VESA)." *Chemical Engineering Journal*., vol.358, no.15, pp.707-717, 2019.

[57] H. V. Thang, L. Grajciar, P. Nachtigall, "Adsorption of CO_2 in FAU zeolites: Effect of zeolite composition" *Catalysis Today*., vol. 227, no.1, pp.50-56, 2015.

[58] L. Feng, Y. Shen, T. Wu *et al.* "Adsorption equilibrium isotherms and thermodynamic analysis of CH_4, CO_2, CO, N_2 and H_2 on NaY Zeolite." *Adsorption*, vol.26, pp.1101-1111, 2020.

[59] B. Xu and L. Kevan "Formation of alkali metal particles in alkali metal cation exchanged X zeolite exposed to alkali metal vapor: control of metal particle identity" *J. Phys. Chem.*, vol. 96, no. 6, pp. 2642, 2645, 1992.

[60] G. Maurin *et al*. "Adsorption of CO_2, CH_4 and their binary mixture in Faujasite NaY: A combination of molecular simulations with gravimetry–manometry and microcalorimetry measurements." *Elsevier*. vol.119, no.1-3, p. 117-128, 2008.

[61] D.B. Shah and D. M. Ruthven, "Measurments of Zeolitic Diffusivities by Chromotography", *AIChE J.*, vol. 23, no.6, pp. 804-810, 1977.

[62] D. M. Ruthven and R. Kumar, "An Experimental Study of Single-Component and Binary Adsorption Equilibria by a Chromatographic Method", *Ind. Eng. Chem. Fundam*. vol.19, no. 1, pp. 27-32, 1980.

[63] A. Henrique, A. E. Rodrigues, J. A. C. Silva, "Separation of Hexane Isomers in ZIF-8 by Fixed Bed Adsorption." *Ind. Eng. Chem. Res.*, vol. 58, pp. 378–394, 2019.

[64] E. Glueckauf, Theory of chromatography *J. Chromatogr. Libr.* vol.*51*, pp. A1–A68, 1955.

[65] F. A. Da Silva, J. A. C. Silva, A. E. Rodrigues, "A General Package for the Simulation of Cyclic Adsorption Processes." *Paracas Art Archit. Object Context South Coast. Peru*, vol. *244*, pp. 229–244, 1991.

[66] A. K. Jakes, S. W. Chai, C. A. Grande, R. Blom, K. A. Andreassen, R. E. Stensrød, M. M. F. Hasan, R.C. Baliban, J. A. Elia, C. A. Floudas, "Numerical analysis of CO_2 concentration and recovery from flue gas by a novel vacuum swing adsorption cycle." *Ind. Eng. Chem. Res.*, vol. 114, pp.1–16, 2012.

[67] M. Bui, C. S. Adjiman, A. Bardow, E. J. Anthony, A. Boston, S. Brown, P. S. Fennell, S. Fuss, A. Galindo, L. A. Hackett, "Carbon capture and storage (CCS): The way forward." *Energy Environ. Sci.*, vol.11, pp. 1062–1176, 2018.

[68] Q. Zhao, F. Wu, Y. He, P. Xiao, P. A. Webley, "Impact of operating parameters on CO_2 capture using carbon monolith by Electrical Swing Adsorption technology (ESA)". *Chem. Eng. J.*, vol.*327*, pp. 441–453, 2017.

[69] R. P. P. L. Ribeiro, C. A. Grande, A. E. Rodrigues, "Electric Swing Adsorption for Gas Separation and Purification: A Review." *Sep. Sci. Technol.*, vol.49, pp. 1985–2002, 2014.

[70] H. Yucel, D. M. Ruthven, "Diffusion in 4A Zeolite." *J.C.S. Faraday* vol. 76, pp.60–70, 1980.

[71] H. Yucel, D. M. Ruthven, "Diffusion of CO_2 in 4A and 5A zeolite crystals." *J. Colloid* Interface Sci., vol. 74, pp. 86–195, 1980.

[72] J. Votruba, V. Hlaváček, M. Marek, "Packed bed axial thermal conductivity." Chem. Eng. Sci. vol.27, pp.1845–1851, 1972.

[73] B.E. Poling, M. Prausnitz, J. P. O'Connell, The Properties *of Gases and Liquids*; Vol.24, 2006.

[74] M. Karimi, Jose L. D. Tuesta, Carmem N. D. P. Gonçalves, H. T. Gomes, A. E. Rodrigues, J. A. C. Silva; "Compost from Municipal Solid Wastes as a Source of Biochar for CO_2 Capture," *Chem. Eng. Technol.*, vol. 43, no. 7, pp. 1336–1349, 2020.

APPENDIX

A- Fixed bed Breakthrough Experiment

After the analysis on the TCD is complete, the data was transferred from "Peak Simple" software from SRI Instruments to Excel. The following is an example on how to treat the data (Run 2.4 at 373 K):

The original signal transferred from "peak simple" is shown in Figure 30. It's a graphical representation of the conductivity (mV) over time (min). The signal is then corrected by eliminating any fluctuations happened before the CO_2 adsorption occurs, as shown in Figure 31.

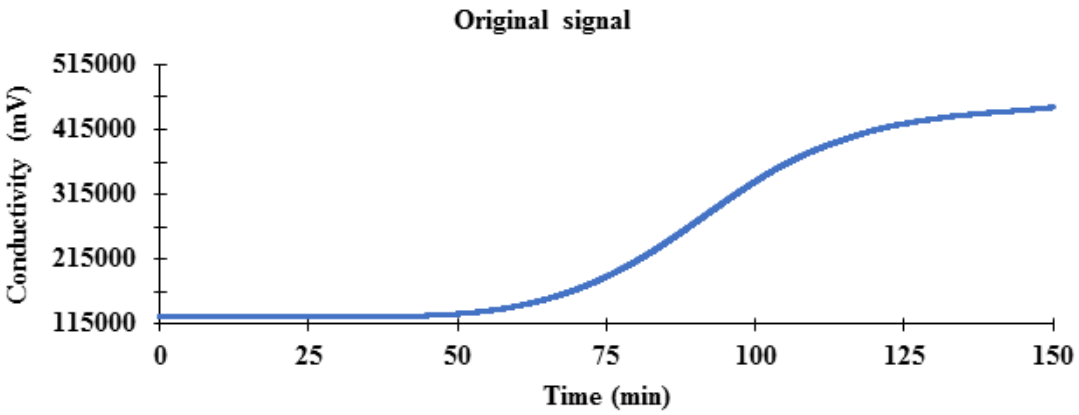

Figure 30: TCD Signal Output

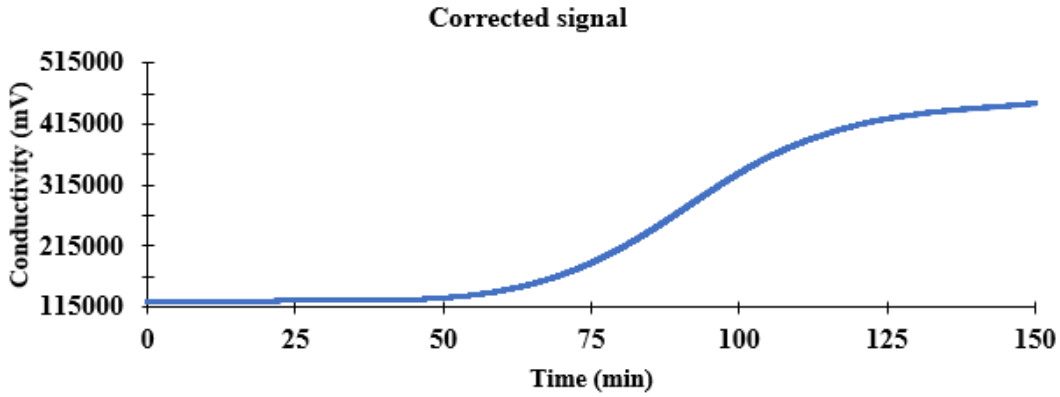

Figure 31: Corrected Signal

The normalized curve was then plotted, which is a graphical presentation of the molar fraction over time (min), as it is shown in Figure 32.

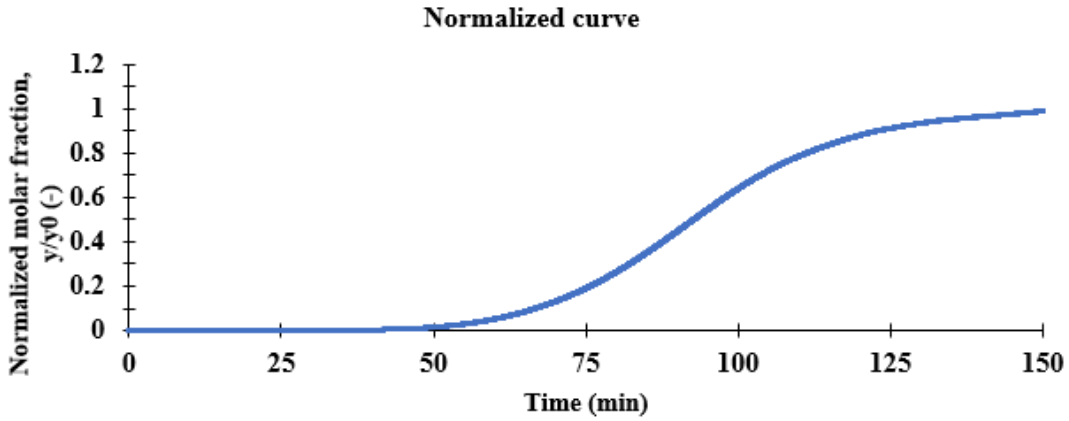

Figure 32: Breakthrough Curve

The area under this breakthrough curve leads us to determining the adsorption capacity. Therefore, by doing a numerical integration using the trapezoidal rule and by applying equation (1):

$$q_i = \frac{1}{m_{ads}}\left(F_{f,i}t_n - \int_0^{t_\infty} F_i dt - \varepsilon_b V_c C_{i0}\right)$$

For Run 2.4:

$$q_{CO_2,run2.4\ (373\ K)} = \frac{1000\ (g/kg)}{26.194\ g}\left(0.000947\ \left(\frac{mol}{min}\right) \times 93.86\ (\text{min}) - 0.0376\ mol\right)$$

$$\boldsymbol{q_{CO_2,run2.4(373\ K)} = 3.36\ mol/kg}$$

B- Determination of Textural Data for binder-free KY Zeolite

Methodology

The textural properties of the materials were determined from N_2 adsorption–desorption isotherms at 77 K, obtained in a Quantachrome NOVATOUCH XL adsorption analyser, following the same procedure as elsewhere [74]. Briefly, the degasification of the catalysts was conducted at 120 ºC during 16 h and then BET, Langmuir specific surface area (S_{BET}, $S_{Langmuir}$) were determined using BET and Langmuir methods. The external surface area (S_{ext}) and the micropore volume (V_{mic}) were obtained by the *t*-method (thickness was calculated by employing ASTM standard D-6556-01). The microporous surface area (S_{mic}) was determined as the subtraction of Sext from S_{BET} and the average pore width (W_{mic}) by approximation ($W_{mic} = 4\ V_{mic}\ S_{mic}^{-1}$). The total pore volume (V_{Total}) was determined at $p/p^0 = 0.98$. Calculations of those methods were all done by using TouchWin™ software v1.21.

Figure 33 shows N_2 isotherms adsorption of the materials. The textural properties of the material are summarized in Table 3.

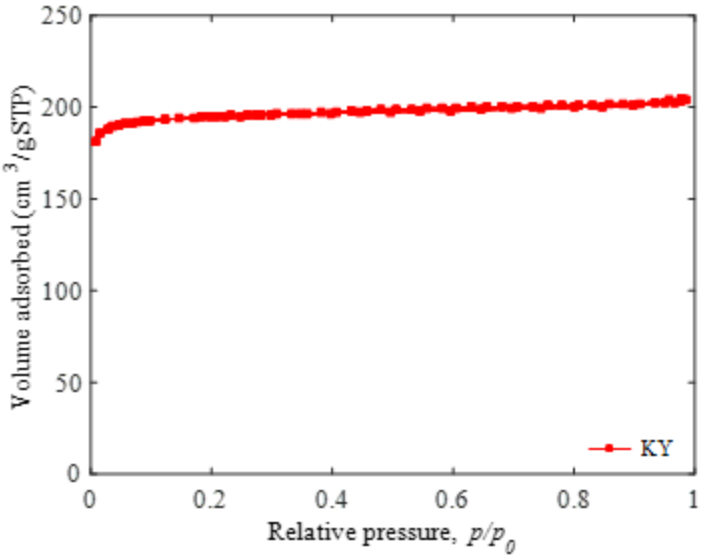

Figure 33: N_2 adsorption-desorption isotherms at 77K of the material.

C- Comparisons of CO_2 adsorption equilibrium data in different ion-exchanged zeolites

Further isotherms comparisons of binder-free KY studied in this work and NaY shown in literature [58, 60] on the adsorption of CO_2 are presented in Figure 34 and Figure 35, where the isotherm goes to the extent of high pressure and where binder-free KY is compared with NaY at different temperatures, respectively. The isosteric heats are also compared with other ion-exchanged zeolites from literature [57] in Figure 36.

As shown in Figure 34 the results are fairly consistent showing that binder-free KY is characterized with better CO_2 adsorption capacity than NaY at low partial pressures. As the pressure increases, NaY becomes more advantageous due to fact that it is characterized with smaller size and therefore the volume occupied is smaller than for KY and hence, it has more space available for adsorption of CO_2 when the pores are reaching saturation.

In Figure 35, it seems visible that binder-free KY demonstrates higher adsorption capacity even at intermediate pressures, but this is only due to the fact that in this comparison, KY is binder-free and NaY isn't. As discussed before, the adsorption capacity of a material can be increased by up to 20% if it is binder-free. Nevertheless, it's been shown already that binder-free KY is a very good alternative adsorbent for the adsorption of CO_2.

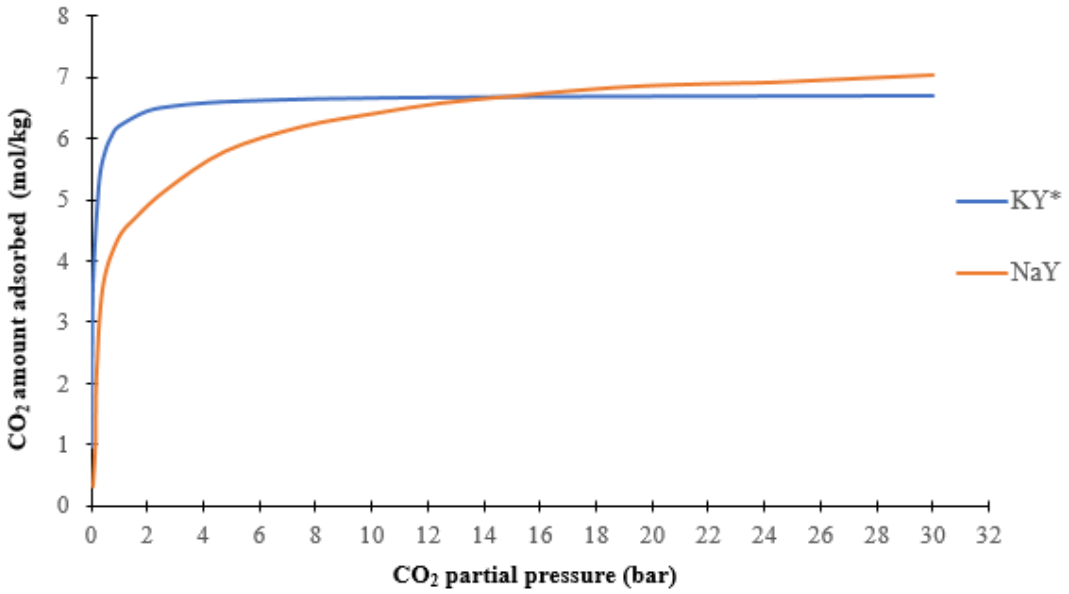

Figure 34: Comparison of CO_2 adsorption isotherms in binder-free KY and NaY at high pressure at 303 K [60].

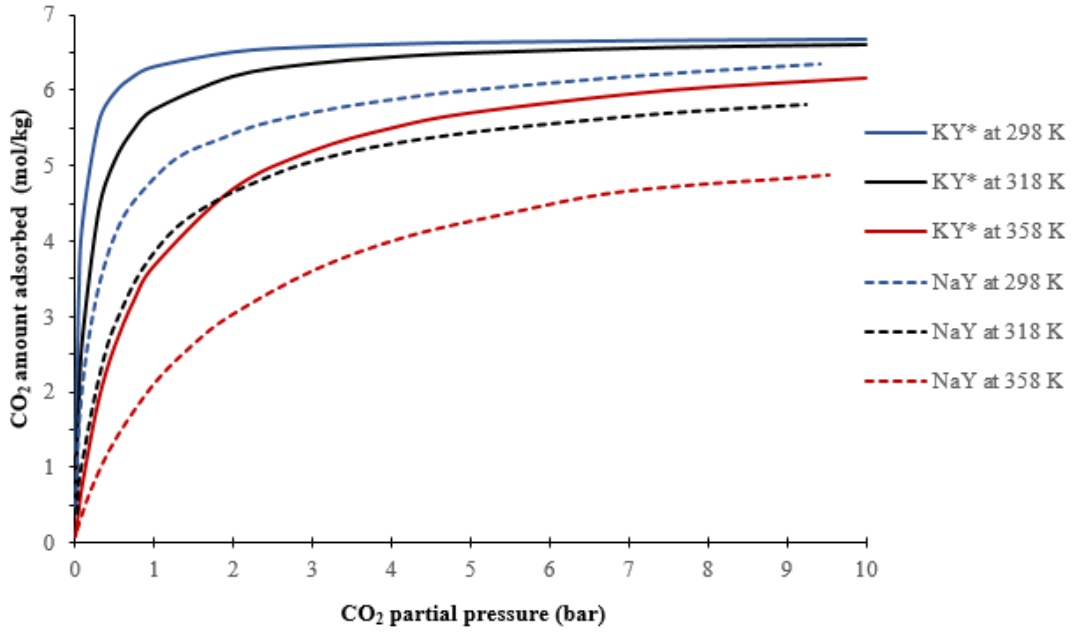

Figure 35: Comparison of CO_2 adsorption isotherms in binder-free KY and NaY at different temperatures [58].

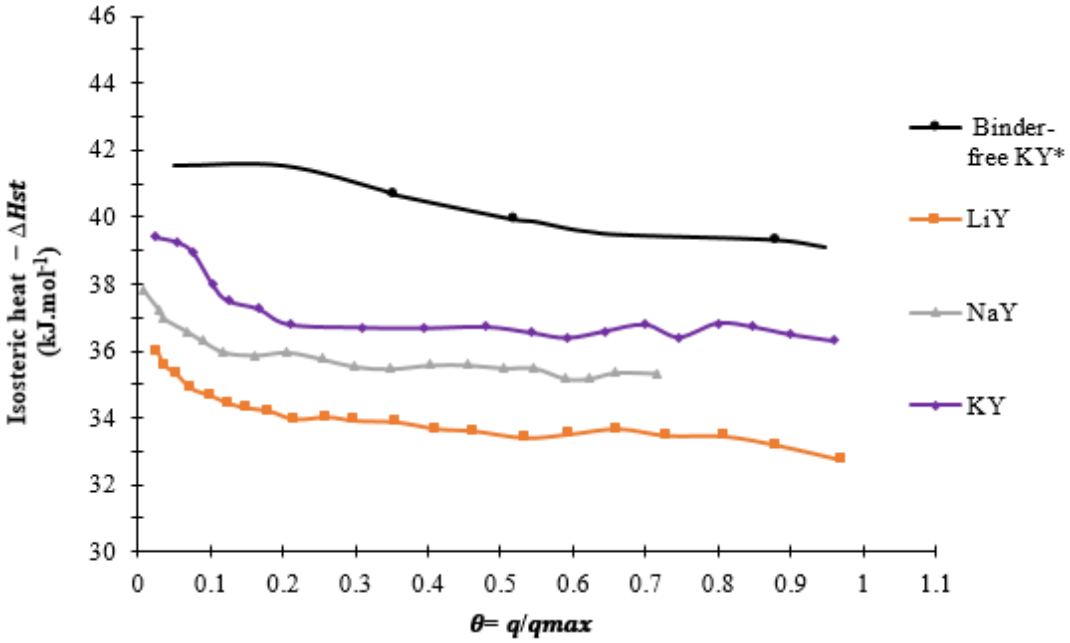

Figure 36: Adsorption heats comparison of CO_2 on alkali-metal exchanged zeolites. [57]

Figure 37 show a comparison between the isotherms collected in this work for binder-free zeolite KY and other binder-free Y zeolites modified by alkali metal cation exchange collected at 298 K, as shown in literature [20].

The results show that the data collected in this work is a lot higher than the one presented in Figure 37. This can be explained by the difference of cation exchange rate, Si/Al ratio as well as different technologies for removing the binder between the two samples.

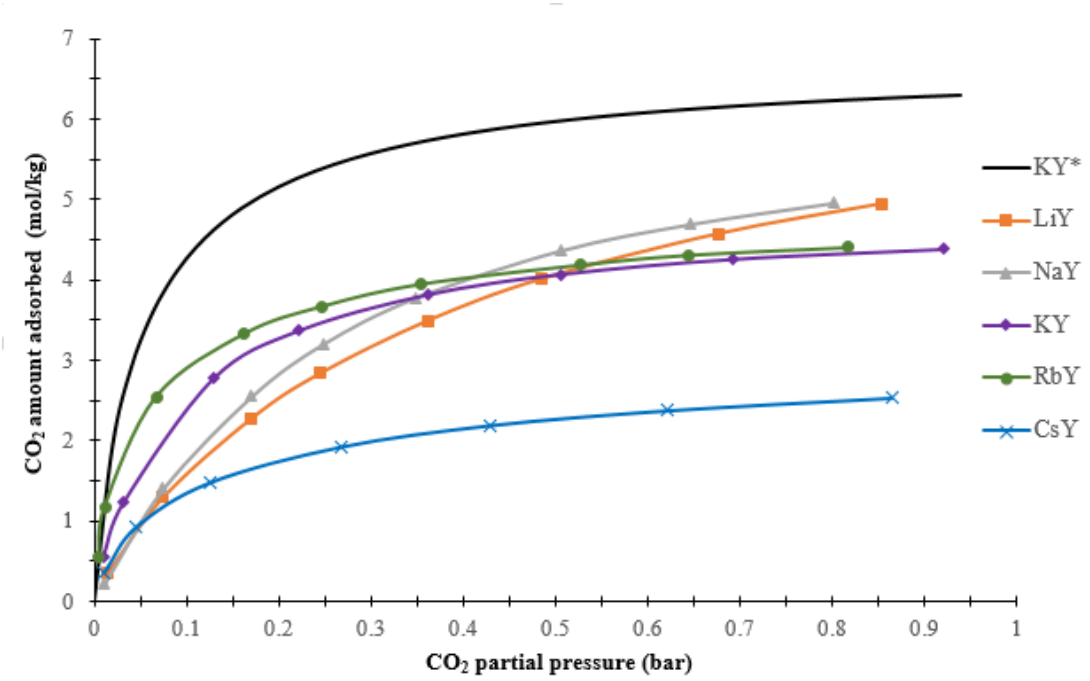

Figure 37: Comparison of CO_2 adsorption isotherms in different binder-free zeolites at 323 K [20].
*The data for binder-free KY was measured in this work.

D- Simulation Correlations

Table 15: Correlations for estimating model parameters used in simulations

D_{ax}	Axial dispersion: $D_{ax} = 0.7D_m + 0.5d_p v_i$. [17]
k_f	The film mass transfer: $Sh = 2R_p k_f / D_m = 2.0 + 0.6Sc^{1/3}Re^{0.5}$ [17]
D_p	Effective macropore diffusivity: $1/D_p = \tau\left(\frac{1}{D_k} + \frac{1}{D_m}\right)$, being tortuosity τ equal 5. [17]
D_c	Intracrystalline diffusivity: estimated through reported values by Yucel and Ruthven. [70,71]
K_{LDF}	Overall mass transfer coefficient: $\frac{1}{K_{LDF}} = \frac{R_p}{3k_f} + \frac{R_p^2}{15\varepsilon_p D_p} + \frac{r_c^2}{15KD_c}$
K_{ax}	Effective axial bed thermal conductivity, $K_{ax} = \left(C_t\ C_{pg} v_i d_p\ \right)/P_{ehp}$, being P_{ehp} taking from Votruba. [72]
h_p	Film heat transfer, $Nu = \frac{2R_p h_p}{\lambda_f} \approx 2.0,\ \lambda_f = C_f D_{AB}$. [17]
C_{pg}	Heat capacity of solid was calculated from correlation available in Poling. [73]